J Therm Spray Tech (2022) 31:745–779
https://doi.org/10.1007/s11666-022-01381-5

REVIEW

Thermal Spraying of Ultra-High Temperature Ceramics: A Review on Processing Routes and Performance

A. Lynam[1] · A. Rincon Romero[1] · F. Xu[1] · R. W. Wellman[2] · T. Hussain[1]

Submitted: 30 September 2021 / in revised form: 11 January 2022 / Accepted: 11 January 2022 / Published online: 4 April 2022

Abstract Ultra-high temperature ceramics (UHTCs) are materials defined as having melting points over 3000 °C and withstand temperatures beyond 2000 °C without losing functionality. As service environments become even more extreme, such materials will be needed for the next generation of aeronautic vehicles. Whether it is atmospheric re-entry or sustained hypersonic flight, materials with resistance to extreme temperature will be in demand. Due to the size and shape limitations encountered by current processing methods of bulk UHTCs research of UHTC coatings, specifically thermal spray UHTC coatings, is accelerating. This paper first presents a general summary of UHTC properties, followed by a comprehensive summary of the processing routes and microstructures of current UHTC thermal spray coatings. Then, a detailed review of the oxidation and ablation resistance of UHTC thermal spray coatings is outlined. Finally, potential avenues for the development of new UHTC coating compositions are explored.

Keywords thermal spraying · plasma spraying · borides · carbides · ultra-high temperature ceramics

Introduction

Ultra-high temperature ceramics (UHTCs) are materials typified by melting points higher than 3000 °C and stability above 2000 °C. This group of ceramics is made up of carbides, borides and some nitrides of group four and five transition metals (Ti, Zr, Hf, V, Nb and Ta); they present strong covalent bonds, which are responsible for the elevated stability at high temperatures.

UHTCs combine stability at extreme temperatures with high hardness, thermal conductivity, elastic modulus, good wear resistance and low coefficient of thermal expansion. Due to the combinations of properties UHTCs possess, they have been under investigation for some time for use in extreme aerospace applications, where inevitably, materials are required to operate at extreme temperatures in oxidizing environments. These applications include rocket propulsion components, leading edges, control surfaces and nose cones for hypersonic flight and atmospheric re-entry craft (Ref 1-5). During sustained hypersonic flight and atmospheric re-entry, operating temperatures can be as high as 2200 °C (Ref 6, 7). With the modern proliferation of private spaceflight companies utilizing reusable craft and the desire to develop hypersonic flight technology for military and commercial purposes, UHTCs have remained materials of significant scientific interest (Ref 8).

While much research in UHTCs has focused on sintered bulk materials, UHTC coatings have also been investigated. UHTC coatings have the advantage of being near net shape while the size and shape of bulk UHTCs are limited by the processing routes needed to densify them (Ref

This invited article is part of a special issue focus in the Journal of Thermal Spray Technology celebrating the 30th anniversary of the journal. The papers and topics were curated by the Editor-in-Chief Armelle Vardelle, University of Limoges/ENSIL.

✉ A. Lynam
alex.lynam@nottingham.ac.uk

T. Hussain
Tanvir.Hussain@nottingham.ac.uk

[1] Coatings and Surface Engineering, Advanced Materials Research Group, Faculty of Engineering, University of Nottingham, Nottingham NG7 2RD, UK

[2] Surface Engineering, Rolls-Royce Plc, Derby DE24 8BJ, UK

9, 10). Using current processing methods, such as spark plasma sintering or hot pressing, such high temperatures and pressures are needed to densify UHTCs that only small, simple shaped components can be fabricated. UHTC coatings have been used to reduce wear in machine parts and bearings, provide oxidation resistance for C or SiC-based composites, provide corrosion resistance and act as diffusion barriers (Ref 11-15). Coatings can be deposited in numerous ways; for example, UHTC coatings have been produced using vapor deposition methods such as physical vapor deposition (PVD) and chemical vapor deposition (CVD) (Ref 14, 16-20). While vapor deposition techniques have been used to form UHTC coatings and have the advantage of creating dense coatings at temperatures below the melting points of UHTCs, these processes can be limited by coating thicknesses ($\sim$20 μm), deposition efficiency and size of the area that can be coated (Ref 21). In order to deposit thick UHTC coatings, thermal spray methods have to be used; however, the extreme melting points and potential for oxidation pose some problems.

This review will focus on thermal spraying of UHTC borides and carbides, specifically TiB_2, ZrB_2, HfB_2, TiC, ZrC, HfC and TaC. The use of UHTCs in cermet (ceramic with a metallic binder) coatings is beyond the scope of this work; however, ceramic–ceramic composites will be discussed. The first section will give a general overview of the physical, mechanical and thermodynamic properties of these bulk UHTCs. The following section will give a brief introduction to various thermal spray processes used to deposit UHTC coatings and how the parameters used within these processes affect the microstructure and properties of UHTC coatings. Of the properties discussed, particular attention will be paid to the high temperature performance of UHTC coatings; the effect of a range of particle reinforcements on the oxidation and ablation resistance of UHTC composite coatings will also be examined. Finally, pathways for the next generation of UHTC coatings will be discussed.

Physical, Mechanical and Thermodynamic Properties of UHTCs

UHTC Borides

As early as the 1960s, at the height of the space race, UHTCs (specifically ZrB_2 and HfB_2) were investigated as solutions for the extreme temperatures encountered in the first generation spacecraft by Kaufman and Clougherty (Ref 22) at the United States Air Force Materials Laboratory. At the same time, in the Soviet Union, similar work was conducted by Samsonov at what is now the Frantsevich Institute for Problems in Materials Science in Kiev (Ref 23, 24). Owing to their excellent thermal and mechanical properties (especially high hardness, high modulus, high thermal conductivity, and low thermal expansion coefficient), UHTC materials were found to be of interest for heat shields, rocket and structural components in these early spacecraft. More recently, these compounds have become subject to increased research for wear resistant applications such as ball bearings, machine tools and engine valves (Ref 25).

Given the success of Kaufman and Clougherty in characterizing the high temperature properties of UHTC borides, much work into UHTCs over the subsequent years was focused on these compounds. Fahrenholtz et al. (Ref 26) provided a detailed summary of the properties of ZrB_2, and HfB_2 while work by Munro (Ref 27) provides similar information for TiB_2. Key physical, mechanical and thermal properties for these materials are outlined in Table 1, where the high melting temperature and hardness can be appreciated (Fig. 1).

The phase diagrams for the Zr-B (Ref 28), Ti-B (Ref 29) and Hf-B (Ref 30) systems are presented in Fig. 2. The phase diagrams show these compounds are formed at the stoichiometric ratio of two boron atoms to every metal atom and are stable up to very high temperatures.

After the value of UHTCs unique combination of properties had been determined, in the 1970s researchers began studies in an effort to understand the oxidation behavior of these materials, with much of the early work in this area again emanating from the Frantsevich Institute in Kiev and the USA (Ref 31, 32). UHTC borides undergo stoichiometric oxidation according to the reaction shown in Eq 1, where M is a group four or five transition metal (Ref 33, 34). UHTC borides form, at temperatures below 1200 °C, a protective liquid B_2O_3 layer. Oxygen diffusion through this protective liquid limits further oxidation. At higher temperatures, the B_2O_3 evaporates, leaving a non-protective porous, metal oxide skeleton leading to rapid oxidation. Due to the higher melting point and low vapor pressure of Zr and Hf oxides (2715 and 2758 °C, respectively), ZrB_2 and HfB_2 have more high temperature resistance than other UHTC borides (Ref 35). To further increase the oxidation resistance of these materials, the addition of silicon carbide (SiC), or other silicon containing compounds (such as $MoSi_2$ or $TaSi_2$) creates a borosilicate glass outer layer which is stable up to temperatures of $\sim$1600 °C (Ref 33).

$$MB_2 + \frac{5}{2}O_2 \rightarrow MO_2 + B_2O_3 \qquad \text{(Eq 1)}$$

Table 1 A comparison of physical, mechanical and thermal properties of ZrB_2, HfB_2 (Ref 26) and TiB_2 (Ref 27)

Property	ZrB_2	TiB_2	HfB_2
Crystal structure	Hexagonal	Hexagonal	Hexagonal
Density (gcm^{-3})	6.08	4.52	11.21
Melting temperature (°C)	3245	3230	3380
Youngs modulus (GPa)	489	565	480
Hardness (GPa)	23	25	28
Fracture toughness (MPa $m^{1/2}$)	3.5-4.2	6.2	…
Coefficient of thermal expansion (K^{-1})	5.9 x 10^{-6}	6.4 x 10^{-6}	6.3 x 10^{-6}
Thermal conductivity (W m^{-1} K^{-1})	60	96	104

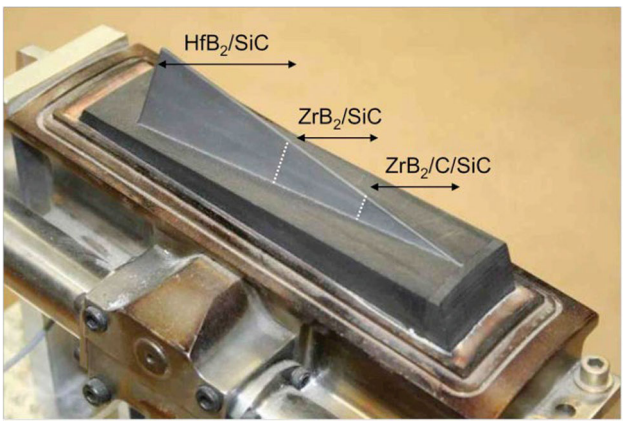

Fig. 1 A strake produced by NASA, for the SHARP-B2 hypersonic research probe, with three different UHTC compositions (Ref 5)

UHTC Carbides

Like UHTC borides, the UHTC carbides were investigated in the 1960s by NASA and various defence agencies and continued through to the 1990s and 2000s for use at high temperatures (Ref 36-39). ZrC has been investigated for various nuclear fuel applications (Ref 40). Carbides, in general, are renowned for their excellent hardness at high temperatures; in fact Miyoshi and Hara (Ref 41) showed that even at 800 °C TiC maintained a microhardness of ~1700 Hv (~17 GPa). Due to their high hot hardness, UHTC carbides have also been used in cutting tool applications (Ref 42, 43).

Key physical, mechanical and thermal properties for the UHTC carbides covered in this review are listed in Table 2. As with the UHTC borides, the hardness and melting points stand out as being extreme. Compared to UHTC borides, the carbides have lower thermal conductivities meaning despite having higher melting temperatures, they are less attractive for use in heat shield applications at ultra-high temperatures. Although UHTC carbides have lower elastic moduli than borides at room temperature, they do maintain their strength at elevated temperatures (> 1000 °C) better than the borides. This means carbides are preferred in applications where higher thermal and mechanical loads are encountered (Ref 44).

Unlike borides, the UHTC carbides are stable across a range of stoichiometries as can be seen in the phase diagrams in Fig. 3 (Ref 53, 54). TiC, ZrC and HfC are all stable between ~37.5 and up to 50 at. % C, while TaC is stable between ~47.5 and 50 at. % C. This range of stable stoichiometries means UHTC carbides have potentially tailorable physical and mechanical properties. As can be appreciated from the data and Table 2 and the phase diagram in Fig. 3, HfC and TaC have some of the highest melting points of all materials.

UHTCs will generally oxidize following the reaction in Eq 2, where M is Ti, Zr or Hf, and Eq 3, where M is Ta (Ref 55-57). In environments with low oxygen pressure, carbon may remain un-oxidized. Oxidation of these compounds can be affected by a number of variables such as chemical composition (it can be seen from the phase diagrams in the previous section that these carbides are not line compounds can present a variety of stoichiometries), grain size and porosity.

$$MC + 2O_2 \rightarrow MO_2 + CO_2 \quad \text{(Eq 2)}$$

$$2MC + \frac{9}{2}O_2 \rightarrow M_2O_5 + 2CO_2 \quad \text{(Eq 3)}$$

As with the UHTC borides, early work on the oxidation of TiC was carried out at the Frantsevich institute in the 1970s (Ref 58). In this study, the authors found that between 700 and 800 °C the lower oxides Ti_3O_5, Ti_2O_3 and TiO formed, but once the temperature was increased to 1200 °C a dense TiO_2 (rutile) scale formed. In studies on HfC and ZrC, oxidation was found to initiate at ~400 °C (Ref 57). At these temperatures, oxidation kinetics are linear, and the formed metal oxide scale remains porous and unprotective. Above 1500 °C, the metal oxide skeleton begins to sinter, and ZrC and HfC show excellent oxidation behavior above 1800 °C when the dense scale can slow down the diffusion of oxygen (Ref 59, 60). Some studies have found that at these low temperatures, an oxycarbide ($Ti/Zr/HfC_xO_{1-x}$) layer forms between the oxide scale and the carbide, limiting oxide diffusion (Ref 40, 58, 61, 62).

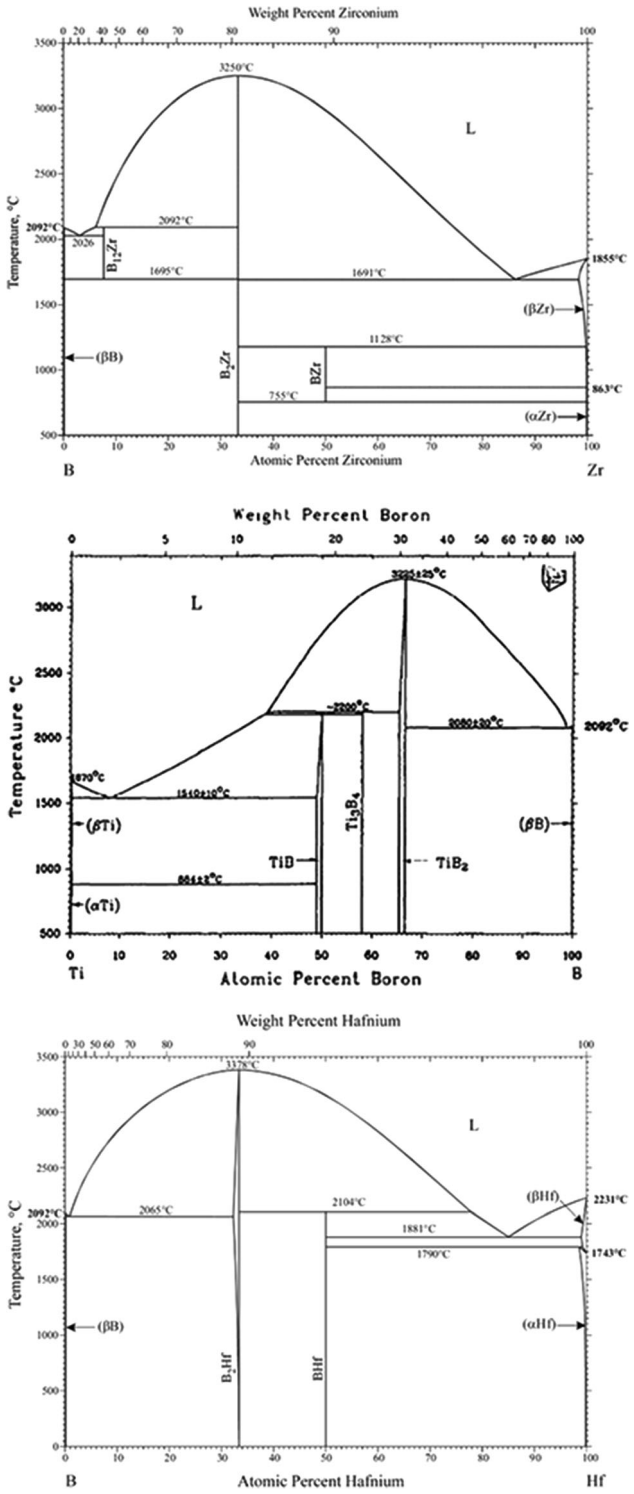

Fig. 2 Phase diagram for the Zr-B (Ref 28), the Ti-B (Ref 29) and the Hf-B systems (Ref 30). Refs 28 and 30 reprinted with permission from Springer Nature. Ref 29 reprinted with permission from John Wiley and Sons

Unlike HfO_2, ZrO_2, which have very high melting points themselves (2715 and 2758 °C, respectively), TiO_2 and Ta_2O_5 have melting points of 1843 and 1872 °C, respectively; hence, their use in high temperature oxidizing environments is limited (Ref 59).

Thermal Spraying of UHTCs

As described previously, the current processing routes for bulk UHTCs, such as spark plasma sintering and hot pressing, limit the size and shapes of components that can be produced. Thermal spraying techniques are already widely used in many industries to coat large areas relatively quickly. This section of the review will focus on the thermal spray processes used in research and their effect on the microstructure, mechanical properties, wear resistance, oxidation and ablation resistance of UHTC coatings.

UHTC Boride Coatings

Deposition and Microstructure of UHTC Boride Coatings

Atmospheric Plasma Spraying Arguably the most versatile thermal spray process is atmospheric plasma spraying (APS). APS uses a radio frequency or, more commonly, direct current arcs to ionize process gases creating a plasma jet. As these unstable plasma ions reform into their gaseous states, a large amount of thermal energy is released, creating extremely high temperatures, up to 14,000 K, within the plasma jet. The primary process gas typically used in APS is argon, with hydrogen, nitrogen, helium or a combination thereof being used as secondary gases to modify the properties of the thermal plasma. Feedstock particles are injected into the gas stream, where particle velocities can be between 20 and 500 mm/s depending on the size of the particle (Ref 63). The extreme temperatures associated with APS mean a wide variety of feedstock materials, including refractory ceramics, can be readily melted. The relatively high particle velocity and high jet temperatures mean that APS can produce coatings with low levels of porosity, high densities and good bond strengths with high efficiency.

Given the high temperatures that are possible within the plasma jet, APS can be used to melt UHTC materials; thus, many researchers have used APS to deposit UHTC boride coatings. Researchers who have used APS to deposit UHTC boride coatings have generally reported coating microstructures with some degree of porosity, partial oxidation of the boride phase and as-sprayed surfaces showing a combination of melted splats and un-melted particles (indicating incomplete melting of the feedstock during the spraying process) (Ref 64-69). For example, in a TiB_2 coating produced by Hong et al. (Ref 68) and a ZrB_2 coating produced by Sun et al. (Ref 69), porosity was measured as being 12 and ~16 %, respectively. Hong et al.

Table 2 A comparison of physical, mechanical and thermal properties of ZrC, TiC, HfC and TaC (Ref 45-52)

Property	ZrC	TiC	HfC	TaC
Crystal Structure	Cubic	Cubic	Cubic	Cubic
Density (gcm^{-3})	6.56	4.94	12.76	14.50
Melting temperature (°C)	3540	3067	3942	3980
Youngs modulus (GPa)	385	451	352	285
Hardness (GPa)	25.5	31.4	24.5	17.5
Fracture toughness (MPa $m^{1/2}$)	2.8	4.6	1.7	3.5
Coefficient of thermal expansion (K^{-1})	6.7 x 10^{-6}	7.7 x 10^{-6}	6.6 x 10^{-6}	6.3 x 10^{-6}
Thermal conductivity (W m^{-1} K^{-1})	21	24	30	22

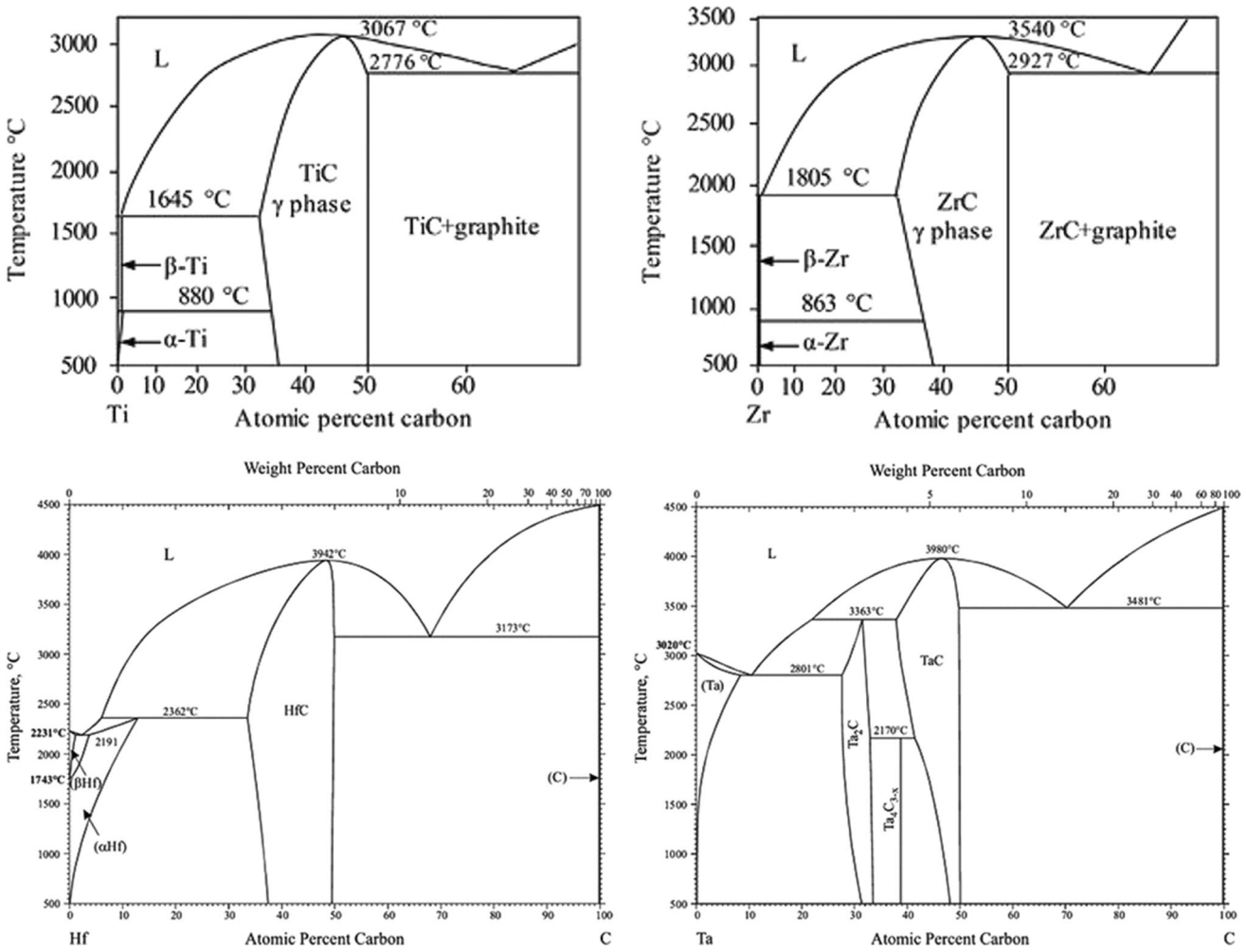

Fig. 3 Phase diagrams for the Ti-C, Zr-C (Ref 53), Hf-C and the Ta-C systems (Ref 54). Ref 53 reprinted with permission from Elsevier. Ref 54 reprinted with permission from Springer Nature

also measured some basic mechanical properties of the TiB_2 coating; Vickers microhardness (0.2 kgf) was measured to be 6.3 GPa. Similarly, the microhardness of a ZrB_2-based coating was measured by Xu et al. (Ref 65) to be 4.91 GPa. In both studies, the reason for the low hardness was suggested to be the degree of porosity.

Using a supersonic APS, designed to create less porous coatings than regular APS, Yao et al. (Ref 70) and Zhang et al. (Ref 71) deposited ZrB_2-based coatings while Li et al. (Ref 72) deposited a HfB_2 coating. In all studies, the coatings showed microstructures with minimal porosity and the as-sprayed surfaces with a combination of melted splats and un-melted particles. XRD diffractograms

showed the boride phases to be dominant but with some Zr/HfO_2.

The influence of spraying power on ZrB_2 coatings has been studied by Hu et al. (Ref 73) and Feng et al. (Ref 66). A ZrB_2 + 20 vol. % LaF_3 composite coating was deposited by Hu et al. at powers of 35, 55, 75 and 95 kW. The authors found that powers of 35 and 55 kW produced coatings with high amounts of un-melted feedstock particles. Porosity was reduced from 31.8 to 16.5 %, 6 and 4.6 %, respectively, as the power was increased; the microstructures of the coatings are shown in Fig. 4. At 95 kW, the residual stresses in the coating caused a certain degree of peeling; hence, 75 kW was found to be the optimum spray power. No difference in phase composition was reported for different coatings with ZrB_2 being the main phase detected, but ZrO_2 and ZrO were also present. Conversely, Feng et al. found that when depositing a ZrB_2-SiC coating at 30, 75 and 97 kW all the coatings were highly porous (58, 43 and 53 % porosity, respectively) regardless of spray power. The coatings deposited at the two higher powers showed a higher degree of fully melted feedstock. ZrO_2 was also detected in the coating deposited at 97 kW while it was not present in the other two coatings.

The particle size of powder feedstocks typically utilized in HVOF thermal spraying and APS is limited between 10 and 100 µm. Using powders of this size ensures the powder particles have enough momentum upon injection to penetrate the middle of the jet, where the highest temperatures are to be found, yet are small enough to melt completely in a very short period of time (Ref 74). Using nano- and submicron scale feedstocks can lead to reducing splat size, reduced porosity and improved properties. To get around this, a technique called suspension thermal spraying has been developed. This is where small particles (<10 µm) are suspended in a liquid, which can flow through the feed system and has sufficient momentum to penetrate the high temperature region of the flame.

Using suspension plasma spraying (SPS), Yvenou et al. (Ref 75) deposited a TiB_2 feedstock with a median particle size of 1.4 µm. XRD results showed no oxide phases present in the coating; however, porosity was high as particles were not melting within the plasma plume.

Plasma Spraying in Inert Atmospheres As discussed in the previous section, when using APS to spray boride-based feedstocks, many researchers have reported the presence of oxide phases in the deposited coatings (Ref 66, 68, 71, 73, 76-78). In fact, an XPS study (Ref 79) of the surface of an APS deposited TiB_2 coating found that Ti and B mainly existed as TiO_2 and B_2O_3 on the surface of the coating. Given the likelihood of interaction between borides and other non-oxide ceramics with oxygen containing atmospheres, spraying systems within controlled inert environments (controlled atmosphere plasma spraying or CAPS), under low atmospheric pressures (low pressure plasma spraying or LPPS) or a vacuum (vacuum plasma spraying or VPS), have been developed (Ref 80).

Controlled Atmosphere and Vacuum Plasma Spraying: The benefits of CAPS and VPS compared to APS were clearly demonstrated by Tului et al. (Ref 81), Kahl et al. (Ref 77) and Niu et al. (Ref 78). In one of the earliest studies on thermal spraying of the material, Tului et al. used APS and CAPS systems to spray ZrB_2 powder. After it had been sprayed into the water (to retain the feedstock as powder after spraying) via both systems, XRD diffractograms of the powder showed the APS technique to have large peak intensity for ZrO_2 phases, indicating a high degree of oxidation during the spraying process. Comparatively, XRD analysis of the powder sprayed by CAPS was shown to have large peak intensity for ZrB_2 phases while

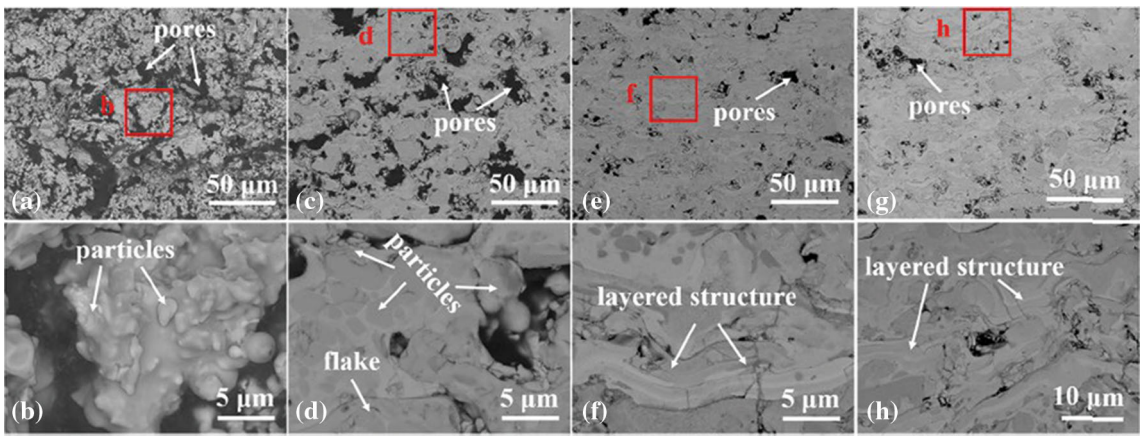

Fig. 4 Microstructures of ZrB_2 + LaF3 coatings produced at different spray powers by Hu et al. (Ref 73) where (a-b) 35 kW, (c-d) 55 kW, (e-f) 75 kW and (g-h) 95 kW. The decrease in porosity as spray power increases is clear. Reprinted with permission from Elsevier

only some ZrO phase was detected. Depending on the spraying parameters used, the microhardness of the coatings deposited using CAPS was in the range of 9.8 to 15.7 GPa with microhardness generally increasing with the power of the torch and pressure inside the spraying vessel. The use of the CAPS system also ensured that the coating microstructures were all dense with minimal porosity. Similarly, Rietveld refinement was used by Kahl et al. to identify and quantify the phases present in APS and CAPS ZrB_2 coatings. Using the CAPS system, with an argon atmosphere, reduces the amount of total oxide phases by 45.7 wt. % compared to the APS coating. The average hardness of the coating was increased from 14.0 to 18.4 GPa using CAPS. Further studies on ZrB_2-based coatings were in agreement that CAPS generally produces coatings with no oxidation of the feedstock and dense microstructures (Ref 82-84). Various room temperature and high temperature mechanical properties of ZrB_2-based coatings were reported by Tului et al. (Ref 82) and Pulci et al. (Ref 83).

Meanwhile, Niu et al. (Ref 78) compared an APS coating to one produced by VPS using a ZrB_2 + 20 vol. % $MoSi_2$ composite feedstock. XRD diffractograms of the two coatings showed the presence of ZrO_2 phase in the coating deposited by APS; the VPS coating showed no oxide phase. The microstructure of the APS coating showed interconnected porosity; meanwhile, the VPS coating had smaller, closed porosities. The porosity was measured as being 9.3 and 6.8 %, respectively. Like CAPS, ZrB_2-based coatings deposited using VPS show no oxidation of the feedstock during spraying; however, these studies measured porosity in the coatings to be as high as ~10 % (Ref 85, 86).

A comparison between LPPS and HPPS ZrB_2-based coatings was made by Bartuli et al. (Ref 87). Characterization of single splats showed distinct morphologies for each process, as shown in Fig. 5. The splats deposited using HPPS show disc-like morphology while the LPPS splats have a branched structure, indicating particles were fully molten when they impacted the substrate. The difference in morphology was due to the higher particle velocities achieved in LPPS, which created splashing as the particles impinged the substrate. The authors suggest that the splats created by HPPS would offer improved cohesive and adhesive strength.

Shrouded Plasma Spraying: In an effort to maintain the inert atmosphere of VPS and CAPS while reducing the cost, some researchers have utilized a technique called shrouded plasma spraying to spray ZrB_2-based coatings (Ref 88-90). Instead of the expensive vacuum and furnace systems required in CAPS and VPS, shroud plasma spraying creates a contained or un-contained Ar or N curtain via an attachment on the end of the plasma torch, limiting the interaction between air and particles within the plasma jet. A detailed study on the effect of various shroud gas flow rates was conducted by Torabi et al. (Ref 90). This work found that increasing the Ar flow rate from 0 l/min (unshrouded) to 30 l/min and finally 150 l/min reduced the ZrO_2 phase content from 41.6 wt. % to 14.5 wt. % to 4.8 wt. %, respectively. Increasing the shroud gas flow also altered the microstructure and splat morphology of the coatings. The unshrouded coating featured many un-melted particles and had a porous microstructure, while increasing shroud gas flow led to a combination of fully melted splats and partially melted particles, as shown in Fig. 6, as well as less porous microstructures (Fig. 7 and 8).

Reactive Plasma Spraying Some researchers have combined self-propagating high temperature synthesis (where constituent elements of a compound are reacted together at high temperatures) or reduction reactions with thermal spraying techniques in what is known as reactive plasma spraying (RPS). During RPS, reactions between precursor particles inside the plasma jet create the desired coating material in situ.

An RPS technique was used by Karuna Purnapu Rupa et al. (Ref 91) to manufacture a ZrB_2 coating. This study used ZrO_2 and 5, 15 and 30 wt. % B_4C precursor feedstocks for the boron carbide reduction reaction, shown in Eq 4, where M is an early transition metal (Zr, Ti, Hf, etc.) (Ref 92). XRD diffractograms of the deposited coatings from Karuna Purnapu Rupa et al. show the relative peak intensity of ZrB_2 is low compared to ZrO_2, suggesting a small proportion of ZrB_2 phase in the coating. The 15 wt. % B_4C feedstock resulted in the highest relative peak intensity of the ZrB_2 phase, however, both 15 and 30 wt. % feedstocks showed the presence of residual B_4C. The ZrB_2 coating had a microhardness of 1.6 GPa, much lower than a ZrO_2 coating sprayed using similar parameters. The low hardness is linked to the highly porous coating microstructures; the authors suggest two reasons for this: unmolten ZrB_2 particles, a consequence of the ZrB_2 particles being formed in situ and having a short residence time in the high temperature plasma jet, or the boron carbide reduction reaction continuing after the coating has been deposited, releasing gases.

$$7MO_2 + 5B_4C \rightarrow 7MB_2 + 3B_2O_3 + 5CO \quad \text{(Eq 4)}$$

Mao et al. used RPS in conjunction with APS and LPPS to manufacture a TiB_2 coating (Ref 93). In this study, Ti and B_4C precursor feedstocks were used, utilizing the self-propagating high temperature synthesis (SHS), to produce a TiB_2-TiC composite coating. Numerous ceramics, including UHTCs, can be synthesized via SHS. At high temperatures (typically 1000-6500 K), the stoichiometric

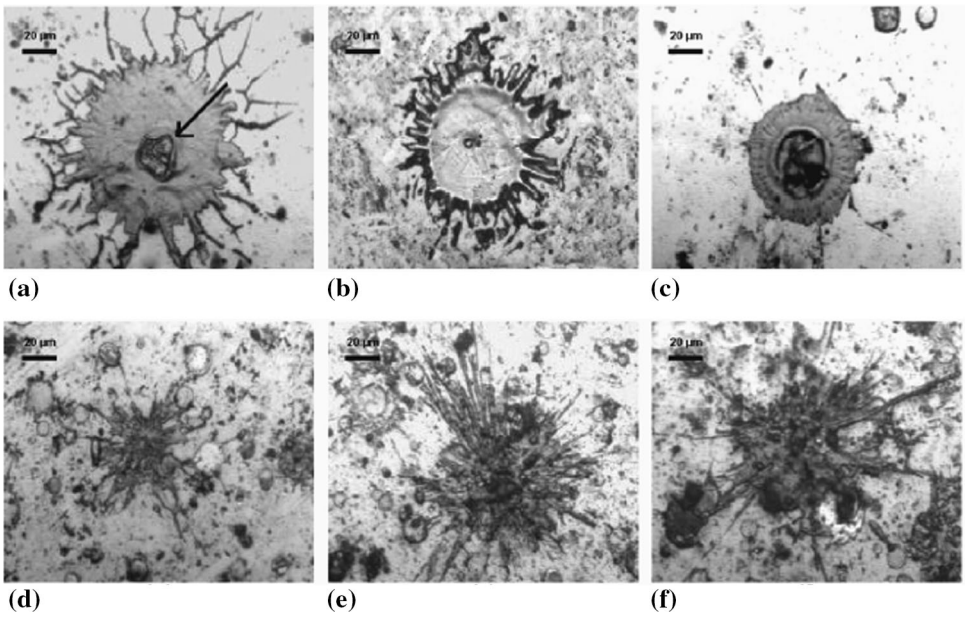

Fig. 5 Optical micrographs of individual ZrB_2 splats produced using HPPS (a-c) and LPPS (d-f) (Ref 87). Reprinted with permission from Elsevier

reaction between constituent elements, in this case Ti and B, becomes thermodynamically favorable in inert atmospheres. SHS relies on the ability of these highly exothermic reactions to be self-sustaining and, therefore, energetically efficient (Ref 94). The use of LPPS eliminated oxidation of the feedstock; the coating had a high degree of porosity; meanwhile, the APS coating had improved density due to the use of Cr as a binder. In terms of composition, the coating produced using APS was made up of TiB_2 and TiN phases with Ti_2O_3 and TiO_2 as well. Comparatively, the LPPS coating was mainly comprised of $TiC_{0.3}N_{0.7}$ and TiB_2 with no oxide phases (the authors suggested residual N remained in the atmosphere despite the low-pressure vacuum). Microhardness values for the LPPS coating were measured to be 4.9 GPa with the low hardness being attributed to the level of porosity in the coating; the corresponding value for the APS coating was 7.1 GPa.

High Velocity Oxy Fuel Thermal Spraying High velocity oxy fuel (HVOF) thermal spraying is a form of flame spraying whereby a gas or liquid fuel (for example, hydrogen, kerosene, acetylene, propylene or natural gas) is ignited in the presence of oxygen. This creates a high temperature, highly pressurized mixture of gases within the combustion chamber into which the feedstock is injected either radially or axially. The feedstock is heated to the molten or semi-molten state within the hot gas stream. A small diameter nozzle accelerates the particles and gas stream to supersonic velocities and directs them towards the substrate. In HVOF thermal spraying, particle velocities can reach 1000 m/s with jet temperatures of approximately 3000 K (Ref 63). Coatings produced by HVOF thermal spraying typically present a lower amount of oxidized phases than coatings produced by plasma spray since the temperatures are lower and the particle velocities are higher. The high impact velocity means HVOF thermal spraying can create coatings with higher densities than other thermal spray processes.

Attempting to prevent oxidation of the feedstock, Cheng et al. used an HVOF thermal spray system to produce a ZrB_2 + 20 vol. % SiC + 10 vol. % $MoSi_2$ composite coating (Ref 95). XRD of the coating showed the presence of no oxide phases. This could be due to the hydrogen/oxygen ratio used in the combustion, where excess hydrogen (3:1 as opposed to stoichiometric 2:1) created a reducing flame (Ref 96). The surface of the coating showed poorly bonded particles indicating the feedstock was not fully melted during spraying.

Table 3 outlines the spraying systems and parameters used in the APS, CAPS, VPS and HVOF thermal spraying studies discussed in this section. Despite various feedstocks, spraying systems and spraying parameters employed, what is clear is that obtaining a dense, oxide free diboride coating is very difficult to achieve without using vacuums or controlled atmospheres.

High Temperature Properties of UHTC Boride Coatings

Many researchers have attempted to characterize the oxidation mechanisms of boride coatings over the years. In one of the earliest studies, TGA analysis of an LPPS coating by Bartuli et al. (Ref 87) found oxidation of ZrB_2 was due to the formation of liquid B_2O_3 at 733 K. At this point, further oxidation is controlled by the rate of diffusion of O_2 through the B_2O_3 layer, see Fig. 9. This work

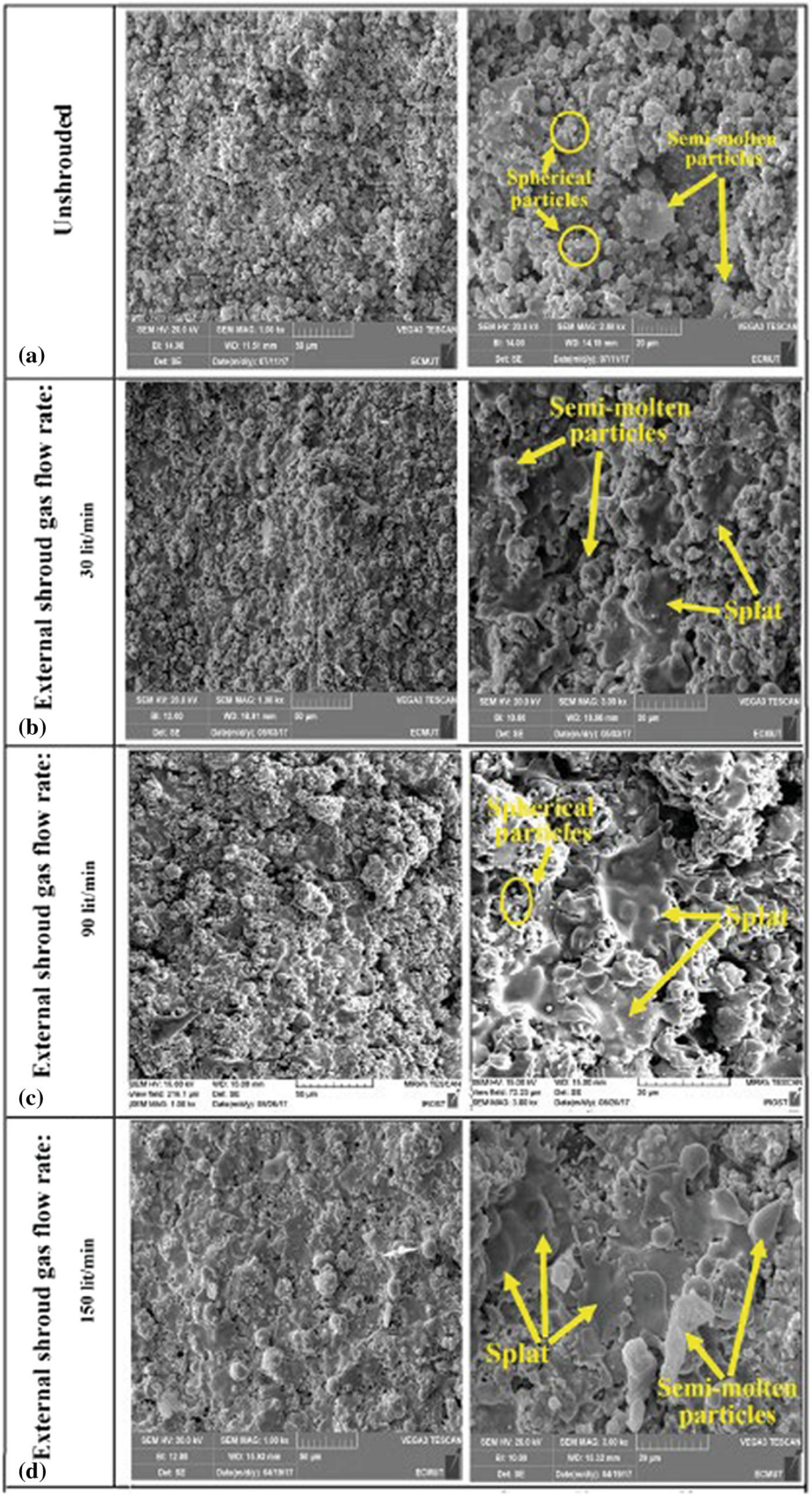

Fig. 6 SEM images of the ZrB_2 coatings produced by Torabi et al. (Ref 90) using (a) no Ar shroud, (b) 30 l/min, (c) 90 l/min and (d) 150 l/min. Note how with increasing Ar flow rate, the amount of un-melted particles decreases and at high Ar flow rates lead to fully molten splats. Reprinted with permission from Springer Nature

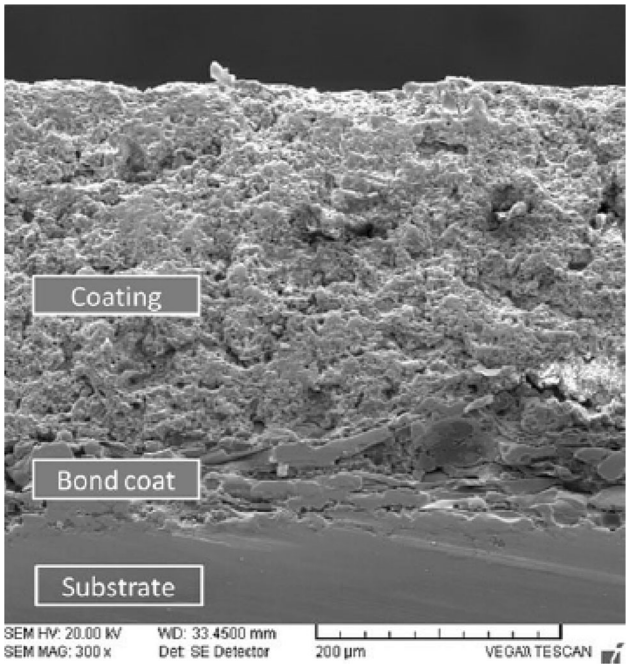

Fig. 7 Cross section of the coating produced by Karuna Purnapu Rupa et al. (Ref 91) on a 304 stainless steel substrate with a nickel-chromium bond coat. Reprinted with permission from Springer Nature

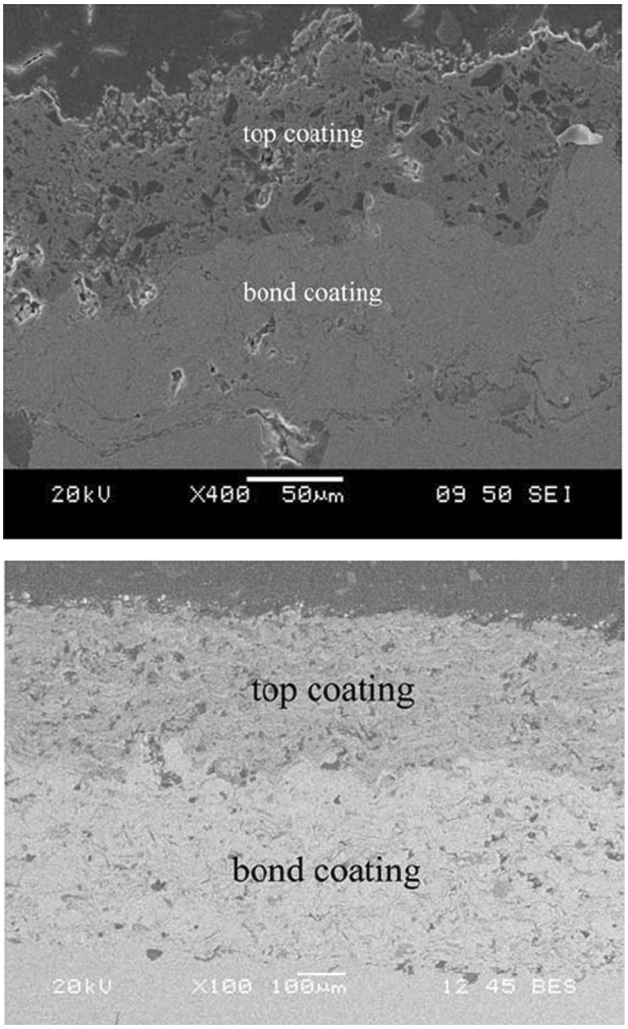

Fig. 8 Cross sections of the coatings produced by Mao et al. (Ref 93). The top image showing the porous coating produced using LPPS. The lower image shows the coating produced using APS. The use of a binder has produced a dense coating. Reprinted with permission from Springer Nature

also showed that the addition of SiC to the ZrB_2 coating could improve the oxidation resistance of the coating. Addition of 25 vol. % SiC led to the formation of silica–boria and borosilicate glasses between 1113 and 1473 K, protecting the coating from further oxidation. Above 1473 K, this layer began to lose its protective properties as B2O3 begins to evaporate.

This mechanism was similarly found in further work on the oxidation of ZrB_2-SiC coatings by Tan et al. (Ref 88) and Alosime et al. (Ref 98). Further to this, Tan et al. also reported an adverse effect on the oxidation resistance of ZrB_2-SiC coatings due to the addition of rare-earth compounds Sm_2O_3 and Tm_2O_3, which reduced the evaporation temperature of B_2O_3. Niu et al. (Ref 78, 85) reported that the same mechanism could be applied to VPS ZrB_2-$MoSi_2$ and ZrB_2-Si coatings, with a thick, protective SiO_2 layer being detected after 6 hours at 1773 K. In comparison, a ZrB_2-$MoSi_2$ coating deposited by APS was found to totally fail after 6 hours; the authors suggested this failure was due to increased porosity within the as-sprayed APS coating, meaning a continuous SiO_2 protective layer could not form. The poor oxidation resistance of APS coatings was further characterized in work by Feng et al. (Ref 66). In this study, three ZrB_2-SiC coatings were deposited using various plasma spray parameters and equipment. Oxidation products were detected after 9 hours at 873 K, with the authors suggesting complete evaporation of B_2O_3 due to its vapor pressure. While after oxidation at 1273 K, the coatings had totally failed.

The addition of AlN to a ZrB_2-SiC coating was investigated by Grigoriev et al. (Ref 67). The coating was subjected to a thermocycling test where the sample was heated to ~2273 K, held for 2 min and then allowed to air cool for 10 min; this was repeated for 15 cycles. The addition of AlN drastically altered the oxidation mechanism of the coating. The authors reported the formation of an Al_2SiO_5-based solid solution around spheroidal ZrO_2 particles, on top of this a protective SiO_2–Al_2O_3 solid solution layer formed, which acted as an effective barrier to the diffusion of O_2. The authors suggested this coating showed excellent stability above 2173 K and offered more protection than typical UHTC coatings.

Table 3 A summary of process parameters for thermal spraying of UHTC boride ceramics

Feedstock	Technique	Particle size (μm)	Spray System	Current (A)	Voltage (V)
ZrB_2	APS	25-75	Praxair SG-100	700	60
ZrB_2	APS	…	…	…	…
	CAPS				
ZrB_2	APS	33.2	Sulzer Metco 9-MB	500-600	…
	CAPS				
ZrB_2-LaF_3	APS	36.5	…	220-512	161-190
ZrB_2-$MoSi_2$	APS	10-60	Sulzer Metco F4-MB	…	…
	VPS				
ZrB_2-SiC	APS	5-10	…	350-385	110-140
ZrB_2-SiC	APS	…	…	350-400	120-150
ZrB_2-SiC	APS	55	Praxair SG-100	185	166
			Progressive Surface 100HE	332	227
				472	205
ZrB_2-SiC-AlN	APS	…	…	…	…
ZrB_2-SiC-SiO_2	APS	30-80	…	950	…
ZrB_2-ZrC/Ni	APS	50-60	Sulzer-Metco F4-MB	…	…
ZrB_2-ZrC-SiC	APS	50-120	Sulzer-Metco F4-MB	550	64
ZrB_2-SiC	CAPS	…	…	…	…
ZrB_2-SiC	CAPS	60	…	…	…
ZrB_2-SiC-$MoSi_2$	CAPS	…	…	…	…
ZrB_2-Si	LPPS	…	Sulzer Metco F4-VB	…	…
ZrB_2-SiC	HPPS	64	Sulzer-Metco F4-MB	…	…
	LPPS		Sulzer-Metco F4-VB		
ZrB_2-SiC	LPPS	…	Sulzer Metco F4-VB	700	…
ZrB_2-SiC-$TaSi_2$					
ZrB_2-SiC	HPPS	60	…	…	…
ZrB_2	Shroud APS	50-150	Sulzer Metco F4-MB	600	…
ZrB_2-SiC	Shroud APS	30-90	…	450	66
ZrB_2-SiC	Shroud APS	38	…	…	…
ZrB_2-SiC-Sm_2O_3					
ZrB_2-SiC-Tm_2O_3					
$ZrO_2 + B_4C$	RPS	<63	Sulzer-Metco 3M	500	50
TiB_2	APS	25	Sulzer-Metco F4-MB	…	…
TiB_2	SPS	1.4	Mettech Axial iii	…	…
$Ti + B_4C$	RPS (APS)	45-75	…	600	35
	RPS (LPPS)				
HfB_2	APS	…	…	400-430	100-150

Table 3 continued

Power (kW)	Primary Gas (Ar) Flow (slpm)	Secondary Gas (H_2) Flow (slpm)	Stand-off Distance (mm)	Coating Phases	Microstructural Features	Reference
42	80	5	100	…	Fine pores, microcracks	64
27-57	30-47	6-16	…	ZrB_2, ZrO_2	…	81
				ZrB_2	…	
40	28-30	12-15	90-150	ZrB_2, ZrO_2	Pores distributed amongst dense lamellae	77
				ZrB_2, ZrO_2	Pores distributed amongst dense lamellae	
35-95	160	80 N_2	100	ZrB_2, ZrO_2, ZrO	Increasing spray power reduced porosity	73
		25-100 H_2				
40	40	10	100	ZrB_2, ZrO_2, $MoSi_2$	Interconnected pores	78 97
				ZrB_2, $MoSi_2$	Fine pores	
…	120-180	60-85	100	ZrB_2, ZrO_2, SiC	Dense microstructure with melted and un-melted particles, pinholes and microcracks on surface	70
…	75	10	100	ZrB_2, ZrO_2, SiC	Dense microstructure with melted and un-melted particles, pores and microcracks on surface	71
30	47	7	100	ZrB_2	Porous microstructure with melted and un-melted particles on surface	66
75	85	42 N_2	150	ZrB_2	Porous microstructure. Un-melted particles on surface	
		42 H_2				
97	85	47 N_2	150	ZrB_2, ZrO_2	Porous microstructure with melted and un-melted particles on surface	
		47 H_2				
…	…	…	…	ZrB_2, SiC, AlN	Dense	67
…	42	24 He	65	ZrB_2, SiC, SiO_2	Dense lamellae containing fine pores	69
…	…	…	…	ZrB_2, ZrC ZrO_2, Ni	Density increased with Ni content	65

Table 3 continued

Power (kW)	Primary Gas (Ar) Flow (slpm)	Secondary Gas (H_2) Flow (slpm)	Stand-off Distance (mm)	Coating Phases	Microstructural Features	Reference
…	35	12	120	ZrB_2, ZrC ZrO_2, SiC, SiO_2	Fine pores with melted and un-melted agglomerates on surface	76
…	…	…	…	ZrB_2, SiC	Eutectic-like fine SiC particles dispersed in ZrB_2 matrix	82
48	55	15	110	ZrB_2, SiC	Dense lamellar	84
…	55	13	…	…	…	83
41	38	10	300	ZrB_2, Si	Dense, lamellar structure with Si distributed inter-granularly within ZrB_2 matrix	85
42	47	9	110	…	…	87
48	25	16	170	ZrB_2, SiC	Dense lamellar	
…	19	6	160	ZrB_2, SiC	ZrB_2 and ZrB_2-SiC eutectic phases with fine pores	86
				ZrB_2, SiC, $TaSi_2$	Dense lamellar, with ZrB_2 and ZrB_2-SiC eutectic and ZrB_2-$TaSi_2$ solid solution phases	
40	500	150	110	ZrB_2, SiC	Fine pores with melted and un-melted particles on surface	98
…	35	14	60	ZrB_2, ZrO_2	Porosity and quantity of un-melted particles decreased with increased shroud gas flow rate	90
…	35	12	80	ZrB_2, ZrO_2, SiC	Porosity caused by un-melted particles	89
…	…	…	…	ZrB_2, SiC	Lamellar with fine pores	88
				ZrB_2, SiC, Sm_2O_3	ZrB_2 and Sm_2O_3 lamellae with SiC particles, pores in between lamellae	
				ZrB_2, SiC, Tm_2O_3	ZrB_2 and Tm_2O_3 lamellae with SiC particles, pores in between lamellae	
…	35	12	100	ZrB_2, ZrO_2, B_4C	Large pores	91
42-47	30-40	9-12	110-130	TiB_2, TiO	Lamellar with fine pores	68

Table 3 continued

Power (kW)	Primary Gas (Ar) Flow (slpm)	Secondary Gas (H_2) Flow (slpm)	Stand-off Distance (mm)	Coating Phases	Microstructural Features	Reference
100	180 (Ar + N2 + H2)	…	50-63	TiB_2	Porosity caused by un-melted particles	75
…	1	1	160	TiB_2, TiN, Ti_2O_3, TiO_2, Cr	Lamellar with fine pores	93
…	75-100	5	100	TiB_2, $TiC_{0.3}N_{0.7}$, Ti_5Si_3, $TiN_{0.3}$, Ti_4N_{3-x}	Porous lamellar	72
				HfB_2, HfO_2	Dense with melted and un-melted particles on surface	

Feedstock	Particle size (μm)	Spray System	Fuel	Oxygen Flow Rate (slpm)	Fuel Flow Rate (slpm)	Power (kW)	Stand-off Distance (mm)	Coating Phases	Microstructural Features	Reference
ZrB_2 + SiC + $MoSi_2$	<15	…	H_2	200	600	66	300	ZrB_2, SiC, $MoSi_2$	Un-melted particles forming porous surface	95

One area where ZrB_2-based coatings have been researched heavily over recent years is to protect carbon-based composites from high temperature oxidation (Ref 99). These composites are ideal for use as high temperature structural components for atmospheric re-entry vehicles due to their excellent high temperature mechanical properties. In use, these components will undergo thermo-chemical ablation due to oxidation at very high temperatures (>1800 °C) and high gas flow rates. However, carbon-based composites will oxidize readily at temperatures above 500 °C; thus, protective, oxidation-resistant coatings are required. Due to the high melting points of their oxides (2700 and 2800 °C, respectively), Zr- and Hf-based ultra-high temperature ceramics have been the main focus of research, as any liquid phases will be removed by the high gas flow rates, reducing the protection of the underlying component.

As explained in previously, the addition of SiC and other Si containing ceramics to ZrB_2 improves the oxidation resistance of the composite. ZrB_2-SiC composite coatings have been produced using thermal spraying, and these coatings are explored for use in protecting graphite, carbon/carbon (C/C) and carbon/silicon carbide (C/SiC) composites.

Yao et al. (Ref 70), Zhang et al. (Ref 71) and Aliasgarian et al. (Ref 89) have all produced ZrB_2-SiC coatings using APS and, in the case of Aliasgarian et al., APS with a N_2 shroud, with feedstocks containing 25, 15 and 20 vol. % SiC, respectively. XRD showed the presence of ZrB_2, SiC, ZrO_2 phases in all the coatings produced in these studies, indicating oxidation of ZrB_2 during the spraying process. In the coatings produced by Zhang et al., a SiO_2 phase was also present, indicating oxidation of SiC; however, this phase was not present in the study by Yao et al. or Aliasgarian et al.

In order to quantify the ablation resistance of these coatings, researchers have subjected them to high temperatures for short periods of time using oxyacetylene torches and, for a given heat flux, linear, and mass ablation rates can be calculated. Using a heat flux of 2.4 MW/m^2, the coatings produced by Yao et al. and Zhang et al. showed mass ablation rates of -0.02 and 0.40 mg/s and linear ablation rates of 0.17 and 0.60 μm/s, respectively. Increasing the heat flux to 4.2 MW/m^2 caused the mass and linear ablation rates of the coating produced by Zhang et al. to increase to 1.97 mg/s and 4.27 μm/s, respectively. Under the same heat flux, the coating produced by Aliasgarian et al. mass and linear ablation rates is 0.0167 mg/s and 0.07 μm/s. The mechanism by which these coatings were protected from ablation was similar for all researchers, with a stable and dense ZrO_2-SiO_2 scale layer forming limiting further O_2 ingress. Zhang et al. found that at 4.2 MW/m^2, with the surface temperature of the test piece reaching

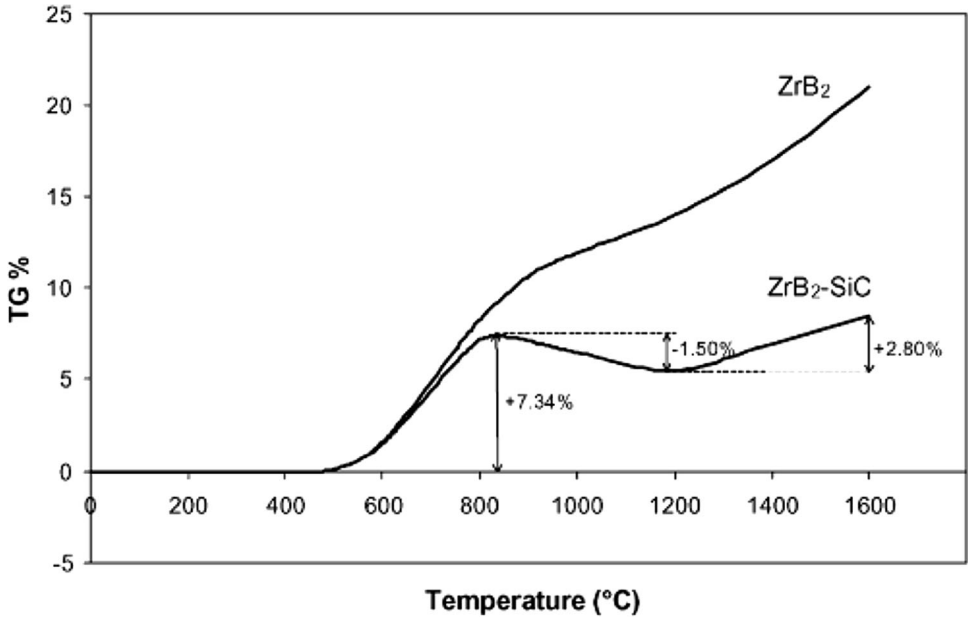

Fig. 9 Thermo-gravimetric analysis of ZrB_2 and ZrB_2-SiC coatings performed by Bartuli et al. (Ref 87) showing % weight change vs. temperature. Reprinted with permission from Elsevier

2523 K, the coating failed. At temperatures of 2400 K and above, the protection afforded by SiC is reduced because of the active oxidation of SiC (forming gaseous SiO) and rapid evaporation of SiO_2 due to its high vapor pressure (Ref 7). The formation of ZrO_2-SiO_2 solution lowers the melting point of ZrO_2, and at high gas flows, this liquid scale is mechanically removed (Ref 100).

Sun et al. (Ref 69) modified the composition of ZrB_2-SiC coatings by adding different volume fractions of SiO_2. Under testing at 1673 and 1973 K, the addition of 30 vol. % SiO_2 was found to be largely resistant to ablation due to the formation of a glassy SiO_2 protective layer on the surface of the test samples. At 2073 K, however, the protective oxide layer was removed by a combination of mechanical action due to the increased gas flow and increased volatilization of SiO_2 due to the increased temperature. Increasing SiO_2 content had no clear effect on the ablation resistance of the coatings at 2073 K.

Rather than ZrB_2, Li et al. (Ref 72) used APS to spray a HfB_2 feedstock. The resulting coating was a combination of HfB_2 and HfO_2 phases. Like the previous works, this coating was subjected to an ablation test at heat fluxes of 2.4 and 4.2 MW/m^2. At 2.4 MW/m^2, the mass and linear ablation rates of the coating were -0.14 mg/s and -0.32 µm/s while at 4.2 MW/m^2 they were 0.26 mg/s and -0.13 µm/s. The high ablation resistance was attributed to the formation of a dense, solid-state HfO_2 layer on the surface of the test piece, which experienced some degree of sintering during the ablation test.

The ablation resistance of ZrB_2 coatings deposited using different flow rates of Ar shrouding gas was tested by Torabi et al. (Ref 90) using a propane torch at a heat flux of 3.0 MW/m^2. Increasing the flow rate of the shroud gas greatly reduced the ablation rates of the coatings, the coating deposited using no shroud had a mass ablation rate of 1857 mg/s while increasing the shroud gas flow rate 150 l/min reduced the ablation rate to 39.3 mg/s. As the shroud gas flow rate was increased, the oxide phase content and porosity of the coating were reduced leading to the greater ablation resistance. The mechanism of ablation from this study is shown in Fig. 10; note how the SiC interlayer also oxidizes and liquid SiO_2 fills the pores created by the oxidation of ZrB_2.

Using LPPS as the deposition method, Wang et al. (Ref 86) found that the addition of $TaSi_2$ to a ZrB_2-SiC composited could effectively reduce the ablation rate. The reasons for the reduction in ablation rate were twofold, the addition of $TaSi_2$ produced a denser coating, and during ablation, a higher fraction of protective glassy SiO_2 phase was produced, which could fill any pores in the oxide scale and prevent subsequent oxidation.

A summary of the ablation tests conducted on UHTC boride coatings is shown in Table 4 where possible the heat flux, surface temperatures and ablation rates have been reported.

Tribology and Wear of UHTC Boride Coatings

The tribology of bulk UHTC borides has been researched widely (Ref 101-106). Despite UHTC borides showing excellent high temperature properties and high hardness, research into their use as wear-resistant thermal spray coatings has been somewhat limited. Tului et al. (Ref 81) performed a pin-on-disc wear test on ZrB_2 coating prepared by CAPS and compared it to WC-Co and Al_2O_3 + TiO_2 (two commonly used wear resistant materials) coatings

prepared by APS and HVOF thermal spraying, respectively. Of all the materials, ZrB_2 showed the lowest COF under an applied load of 80 N, indicating that ZrB_2 could be an excellent material for wear resistant thermal spray coatings. Xu et al. (Ref 65) subjected composite ZrB_2-ZrC APS coating to a wear test against abrasive SiC paper, under loads of 5, 10 and 20 N giving wear rates of 3, 4 and 7 $x10^{-10}$ m^3m^{-1}, respectively.

A TiB_2 coating produced by Hong et al. (Ref 68) was subjected to wear test under 20 and 50 N loads against a WC-Co ball giving COF of 0.72 and 0.50 and wear rates of 27.1 x 10^{-5} and 63.2 x 10^{-5} mm^3 N^{-1} m^{-1}, respectively. The wear mechanisms were described as adhesive, fatigue and tribo-oxidation under both sets of conditions.

UHTC Carbide Coatings

Deposition and Microstructure of UHTC Carbide Coatings

Atmospheric Plasma Spraying As with the boride coatings discussed earlier, due to the extreme melting points of UHTC carbides, plasma spraying is the most popular deposition technique. In the 1980s and 1990s, APS TiC coatings were investigated to protect nuclear fusion device components from thermal shock (Ref 107-112). Some of these early coatings suffered from high porosity, oxidation and decarburization (Ref 110, 113, 114).

More recently, a detailed characterization of a TiC APS coating was carried out by Hong et al. (Ref 68, 115). The phases present in the coating were quantified as being 87 wt. % TiC, 9 wt. % TiO_2 (rutile) and 4 wt. % TiO. Porosity was measured at 8.0 %. As with previous studies, the as-sprayed surface showed melted and un-melted particles while the microstructure was largely dense and well bonded with some microcracks caused by stresses upon cooling. Hardness and elastic modulus were also measured for this coating, 7.7 GPa and 189.7 GPa, respectively. The authors suggested that these mechanical properties were lower than reported for bulk ceramics because of porosity levels, inter-splat strength and phase composition.

Mahade et al. (Ref 116) deposited a TiC feedstock with a median particle size of 2.21 µm using SPS. The XRD diffractogram of the coating showed the main phases were titanium oxycarbide ($TiC_{0.1}O_{0.9}$), TiC and Ti_2O_3 with smaller peak intensities of TiO_2 (both anatase and rutile). The as-sprayed surface of the coating showed very fine ($\sim$3 µm) melted splats and some un-melted particles. The microstructure revealed uniformly distributed porosity, a few un-melted particles and good adhesion between splats, see Fig. 11.

When depositing ZrC coatings with APS, researchers have typically found a small degree of oxidation with ZrC forming monoclinic and tetragonal ZrO_2 with small relative peak intensities relative to ZrC when characterized with XRD (Ref 117-120). Generally, decarburization has been minimal; however, other works have found more severe oxidation of ZrC with relatively large peak intensities of ZrO_2 and other oxidation products detected (Ref 121, 122). Interestingly, in a study by Wu et al. (Ref 123), XRD detected small peak intensities of cubic ZrO_2. Cubic ZrO_2 is formed above 2370 °C, whereas between 1170 and 2370 °C tetragonal is the stable phase (monoclinic being formed below 1170 °C). The presence of this phase could indicate higher temperatures were achieved in the plasma plume using this set of parameters compared to the other studies. The coating microstructures produced in all these studies are similar, with the surface showing a combination of melted and un-melted splats and the cross-sectional microstructure appearing fairly dense with minimal pores; a typical example from Wu et al. is shown in Fig. 12. Fewer studies have investigated APS of HfC coatings, but the results were similar (Ref 124-126). During spraying, some oxidation of HfC was reported, the microstructures of the coatings were dense, and the as-sprayed surfaces showed some melted and un-melted splats.

Controlled Atmosphere and Vacuum Plasma Spraying As with thermal spraying of most non-oxide ceramics, researchers have turned to spraying in inert atmospheres or vacuums to protect the feedstock from oxidation. A comparison between APS and VPS ZrC coatings was made by Hu et al. (Ref 97). The XRD diffractograms of the two coatings showed the VPS contained only the ZrC phase, while the APS coating contained ZrC, Zr_2O and ZrO oxide phases, further testing revealed the VPS coating contained 0.7 wt. % O while the APS coating contained 3.3 wt. %. The as-sprayed surfaces of both coatings contained mainly melted splats, while more porosity was visible on the surface of the APS coating. Cross-section microstructures showed the APS coating made up of a lamellar structure of alternating ZrC (light phase in Fig. 13) and Zr_2O/ZrO layers (darker layers). The microstructure of the VPS coating was shown to be made up of lamellar columnar crystals mainly containing ZrC phase, as shown in Fig. 14. Porosity was also reduced by using VPS, from 12.1 to 3.3 %.

Subsequent studies of VPS ZrC-based coatings returned similar findings, with the ZrC phase being entirely retained during spraying, as-sprayed surfaces appear as a combination of melted and semi-melted splats and dense microstructures with minimal porosity (Ref 127-132). Pan et al. (Ref 132) found the properties of a ZrC-SiC coating could be achieved if the feedstock powder was spheroidized using induction plasma spheroidization (IPS). Compared to agglomerated powder prepared by spray drying (SD), with the use of IPS a higher degree of melting

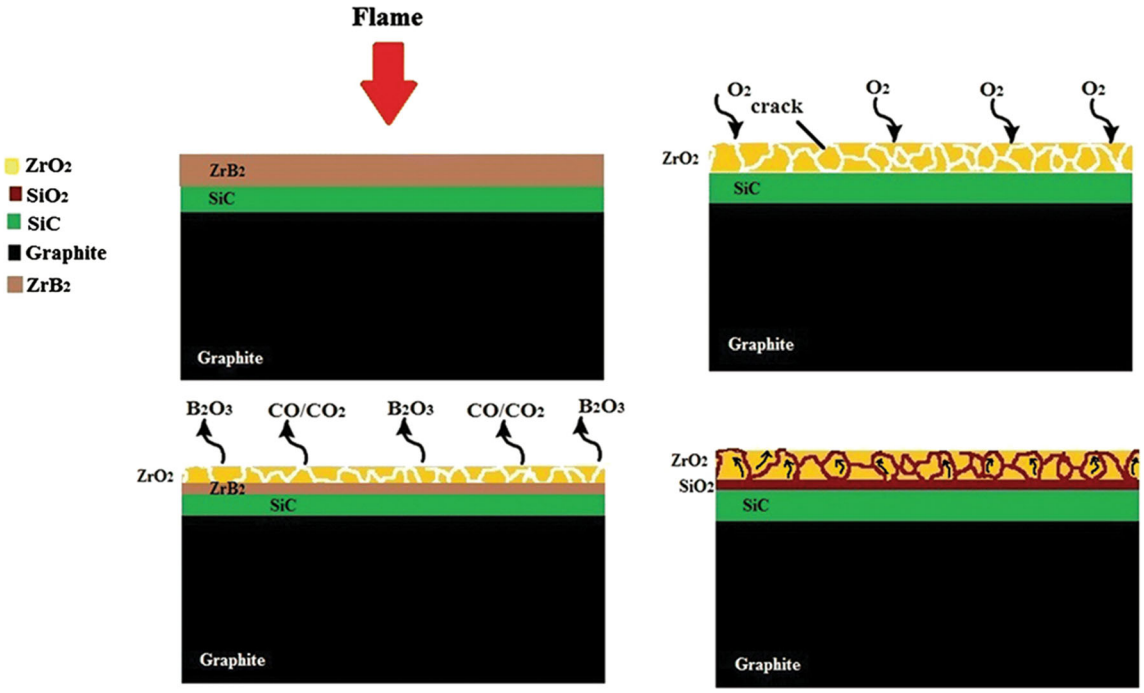

Fig. 10 Schematic diagrams showing the ablation mechanism of a ZrB_2-SiC multi-layer coating. Note the diffusion of liquid SiO_2 from the interlayer to protect from further oxygen diffusion (Ref 90). Reprinted with permission from Springer Nature

was observed on the as-sprayed coating surface, porosity was reduced from 10.7 to 4.6 %, and deposition efficiency was increased.

In an early study, Varacelle et al. (Ref 133) investigated the effect of three VPS parameters on TiC coatings, specifically arc current, primary gas flow and secondary gas flow, using a Taguchi style design of experiment. The lowest porosity (0.49 %) and highest hardness (9.4 GPa) were found in the coating deposited using the highest power to gas flow volume ratio, meaning high spray powers and relatively low primary gas flows led to a greater degree of melting of the TiC feedstock, better deposition efficiency and less porosity. In another early study, the effect of Ar and N_2 atmospheres on CAPS TiC coatings was investigated (Ref 134). Minimal differences were noted between the two atmospheres; the microstructures appeared similar, the hardness of the coatings was similar (12.5 GPa for Ar and 12.75 for N_2), and the decarburization was minimal in both cases. This led the authors to believe, when spraying TiC in a controlled atmosphere, the cheaper N_2 gas could be used.

Despite using VPS, Guo et al. (Ref 135) found TiC coatings to have relatively high levels of porosity (8.6 %), a high fraction of un-melted particles and a hardness of 6.0 GPa. They found that adding 20 vol.% Mo to create a composite TiC-Mo coating effectively acted as a binder, reducing porosity to 4.8 %. The hardness was similar to the pure TiC coating at 6.1 GPa. TEM analysis found a (Ti, Mo)C transition phase between TiC parallel columnar grains and Mo splats that improved the bonding in the coating. Finally, a multilayer HfC/TiC multilayer coating was produced by Kim et al. (Ref 136). Both layers were dense and well bonded to each other.

In the 1990s, HfC was researched as an oxidation protection coating for C- and SiC-based composites. Most of the coatings were produced by vapor deposition methods; however, Boncoeur et al. (Ref 137) used CAPS to produce a dense oxide free HfC coating. Subsequently, HfC- and HfC-based composite coatings have been deposited by numerous researchers using VPS (Ref 124-126, 138). These coatings show similar features, no decarburization or oxidation during spraying, a combination of un-melted and fully melted splats on the as-sprayed surface and dense microstructures. Yoo et al. (Ref 139) used suspension vacuum plasma spraying (SVPS) to deposit a HfC feedstock with a median particle size of 7.08 µm. Due to the density of HfC; the powder had to be further crushed to ~200 nm particle size in order to make a stable suspension. Using a suspension with 20 wt. % solid loading a coating of ~50 µm was produced. Despite spraying in a vacuum, the XRD diffractogram of the coating presented with large relative peak intensities for HfO_2, which was attributed to oxygen present in the ethanol in which the HfC particles were suspended.

VPS has also been used to deposit TaC and TaC-based composite coatings. Researchers have noted the formation

Table 4 A summary of high temperature tests conducted on UHTC boride coatings

Feedstock	Deposition method	Duration (s)	Ablation test Type	Heat flux (MW/m^2)	Flame temperature (K)	Surface temperature (K)	Mass ablation rate (mg/s)	Linear ablation rate (um/s)	Reference
ZrB_2	APS	60	Propane flame	3.0	…	2473	1857	…	90
	Shrouded plasma spray - 30 l/min						735		
	Shrouded plasma spray - 90 l/min						353		
	Shrouded plasma spray - 150 l/min						39.3		
ZrB_2 + 15 vol. % SiC	APS	60	Oxyacetylene flame	2.4	…	2173	0.4	0.6	71
				4.2		2523	1.97	4.27	
ZrB_2 + 20 vol. % SiC	Shrouded plasma spray	60	Oxyacetylene flame	4.2	…	2207	0.0167	0.07	89
ZrB_2 + 25 vol. % SiC	APS	…	Oxyacetylene flame	2.4	2273	…	−0.02	0.17	70
ZrB_2 +SiC	LPPS	600	Oxyacetylene flame	…	…	…	0.689	…	86
ZrB_2 + SiC +$TaSi_2$							0.114		
ZrB_2 + 20 vol. % SiC +10 vol. % $MoSi_2$	HVOF	40	CO_2 laser beam	250	…	…	…	90	95
ZrB_2 + 22 vol. % SiC + 10 vol. % SiO_2	APS	6000	Oxyacetylene flame	…	…	2073	0.34	…	69
ZrB_2 + 20 vol. % SiC + 20 vol. % SiO_2							0.667		
ZrB_2 + 17.5 vol. % SiC + 30 vol. % SiO_2							0.83		
ZrB_2 + 15 vol. % SiC + 40 vol. % SiO_2							0.667		
HfB_2	APS	30	Oxyacetylene flame	2.4	…	2273	−0.14	−0.32	72
				4.2		2623	0.26	−0.13	

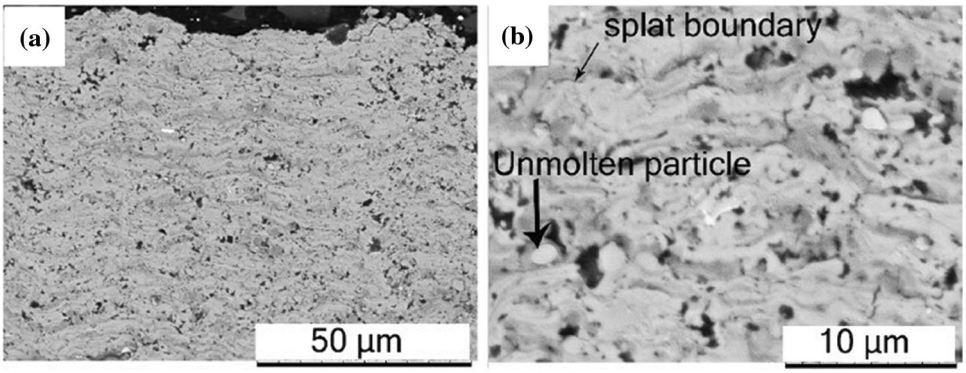

Fig. 11 Low magnification (a) and high magnification (b) SEM micrographs of SPS deposited TiC coating (Ref 116)

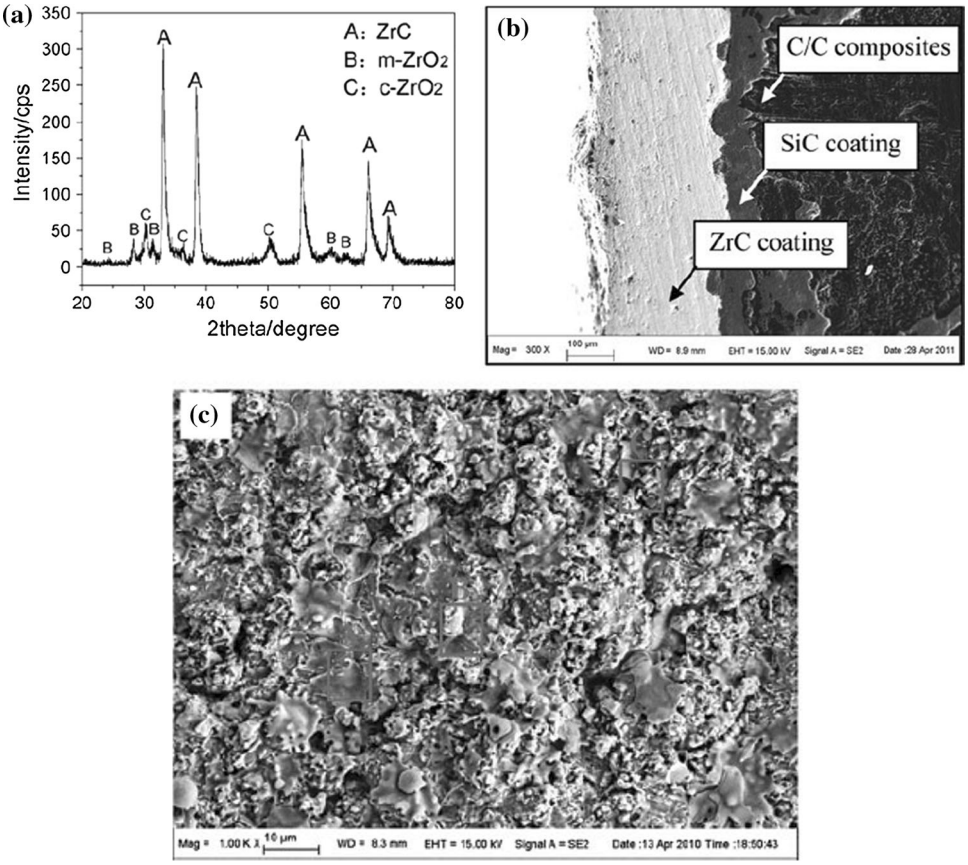

Fig. 12 A diffractogram (a), microstructure (b) and as-sprayed surface (c) of a ZrC coating (Ref 123). The microstructure appears to have minimal porosity while the as-sprayed surface shows a combination of melted and un-melted splats. Reprinted with permission from Springer Nature

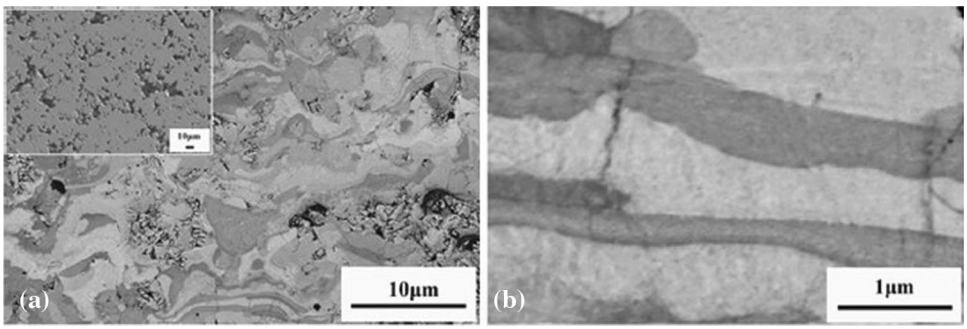

Fig. 13 SEM micrograph of an APS ZrC coating at (a) low magnification and (b) high magnification (Ref 97). The lamellar microstructure is clearly visible. Reprinted with permission from Springer Nature

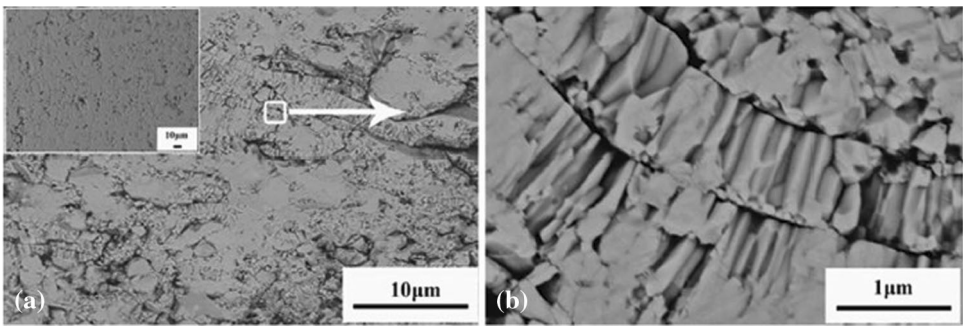

Fig. 14 SEM micrograph of a VPS ZrC coating at (a) low magnification and (b) high magnification (Ref 97). The lamellar microstructure and columnar crystals are clearly visible. Reprinted with permission from Springer Nature

of Ta_2C phase when characterizing these coatings (Ref 140-144). Balani et al. (Ref 140) calculated that the Gibbs free energy of formation was lower for Ta_2C than TaC hence its formation during VPS. Schulz et al. (Ref 142) proposed two possible reasons for this; thermodynamically favorable formation of hydrocarbons between the carbide powder and plasma gases or the higher vapor pressure of carbon relative to tantalum which would indicate a favorable loss of carbon during the spraying process. In general, however, the microstructures were similar to what has been reported for other UHTC carbides, with a combination of un-melted and fully melted splats on the as-sprayed surface and dense microstructures.

High Velocity Oxy Fuel Thermal Spraying Researchers have also used HVOF thermal spraying to deposit TiC coatings, Srinath et al. (Ref 145) deposited a TiC + 10 wt. % Cr_2O_3 feedstock using this process. Even using HVOF thermal spray to deposit the coating the as-sprayed surface shows a combination of fully melted splats and some un-melted granules, which the authors identified as Cr_2O_3. Unfortunately, the authors did not present a clear XRD diffractogram to identify the phases present. Förg et al. (Ref 146) also used HVOF thermal spray to deposit a TiC coating, this time using a suspension of TiC particles between 2 and 3 μm in size in water. This study used three water-based suspensions; one comprised of 20 wt. % of TiC powder, the second containing 20 wt. % milled TiC powder, and the final containing 20 wt. % of the powder with an added dispersant and the pH adjusted in an effort to make a more stable suspension. During spraying all the feedstocks experienced significant oxidation, XRD diffractograms identified the main phases present in all of the coatings as being TiO_2 (rutile and anatase) and TiC. SEM images of the as-sprayed surface also showed a combination of melted and un-melted particles. The microstructure was mainly dense with some carbide pull-out and microcracking. The coating produced from the first suspension (TiC powder and water) had the lowest porosity, 1.9 %, and the highest hardness, 5.2 GPa.

Table 5 outlines the spraying systems and parameters used in the APS, CAPS, VPS and HVOF thermal spraying studies discussed in this section.

High Temperature Properties of UHTC Carbide Coatings

As with UHTC boride coatings, one area where UHTC carbide coatings have potential applications is in the protection of carbon-containing composites. Thus, the high temperature properties, namely the ablation resistance, of these carbide coatings have been widely researched.

The behavior of ZrC coatings, when subjected to ablation by oxyacetylene torch, has been studied by Wu et al. (Ref 123), Jia et al. (Ref 117-120), Kang et al. (Ref 128) and Liu et al. (Ref 129). Despite different deposition methods, the mechanism of ablation described by the authors was largely similar. In all cases, the only phase detected after ablation testing was monoclinic ZrO_2. At high temperatures, ZrO_2 will have a tetragonal or even cubic crystal structure, but upon cooling, it will transition to the monoclinic phase; the volume change associated with this phase change has resulted in the formation of cracks after testing, while escaping CO and CO_2 gases due to the oxidation process created pores.

While the mechanism reported in these studies was similar, interestingly, some of the results were different. Jia et al. (Ref 117) demonstrated the evolution of an APS ZrC coating after ablation for different periods of time. After 90 seconds of 2.4 MW/m^2 heat flux, the ZrC had failed completely, exposing the SiC interlayer beneath to oxidation. The microstructures after 30 and 60 seconds appear porous, likely due to gas release, see Fig. 15. The authors suggest that this allowed O_2 to diffuse through the ZrO_2 scale and oxidize the SiC interlayer, consuming it and removing any adhesion between the layers. The high gas flow rate then caused the total removal of the oxidized coating. The authors reported a similar porous microstructure (albeit without the total removal of the coating) in a further ablation study, this time at 4.2 MW/m^2 for 15 seconds (Ref 118). A porous structure was also

noted by Liu et al. (Ref 129), this time with a coating deposited using VPS.

Alternatively, coatings produced by Wu et al. (Ref 123) and Kang et al. (Ref 128) using APS and VPS, respectively, present mainly dense microstructures after ablation testing, see Fig. 16, with some pores and microcracking attributed to gas release and ZrO_2 monoclinic transformation, respectively. In both studies, the authors suggested this was due to the complete melting of ZrO_2 in the ablation centre (despite Kang et al. reporting the maximum temperature only reaching 2325 K, well below the melting point of ZrO_2).

A comparison between the ablation resistance of VPS and APS deposited ZrC coatings was made by Hu et al. (Ref 97). The VPS coating offered better protection to ablation due to its less porous microstructure and lower oxidation during spraying, allowing a dense ZrO_2 layer to be formed during ablation.

In order to improve the ablation resistance of ZrC coatings, many researchers have focused on the additions of other materials to form composites. Similar to UHTC boride coatings, Si-containing materials such as SiC and $MoSi_2$ are common additives to carbide composite coatings, as it forms a protective SiO_2 layer at high temperature. Jia et al. (Ref 118, 120), Yao et al. (Ref 121), Liu et al. (Ref 127, 129) and Pan et al. (Ref 130-132) have all tested ZrC-SiC composites using various ablation tests. When compared to a ZrC coating, Jia et al. (Ref 118) reported no benefit of SiC addition under ablation at 4.2 MW/m^2 for 15 seconds. The authors suggested that due to the high temperature, active oxidation of the SiC prompted a massive release of gases, causing many pores to be formed in the coating. A similar result was obtained by Yao et al. (Ref 121) using a multilayer coating made up of ZrC top layer with a ZrC-SiC layer underneath. Due to extreme temperatures, the ZrC became molten and exposed the ZrC-SiC layer below, causing volatilization of SiO and the formation of many pores on the surface of the coating.

A more thorough investigation into the mechanism by which SiC addition can improve the ablation resistance of ZrC-based coatings was conducted by Jia et al. (Ref 120). In this work, a ZrC composite coating containing 20 vol. % SiC was subjected to ablation testing at three temperatures under a heat flux of 2.4 MW/m^2. At 2011 K, a glassy SiO_2 phase was formed, encapsulating the ZrO_2 and protecting the structure from further oxidation. When the temperature was increased to 2378 K, SiO_2 evaporated, leaving behind a porous, unprotective ZrO_2 coating, and the linear ablation rate increased to 2.5 µm/s, and the mass ablation rate was 0.49 mg/s. However, as the temperature was increased further to 2543 K, the authors suggest the temperature was high enough for the composite oxide ZrO_2-SiO_2 to be semi-molten, even as SiO_2 was evaporated. The semi-molten phase offers protection from further oxidation and is viscous enough not to be removed mechanically by the gas stream. In one final experiment, the authors increased the heat flux to 4.2 MW/m^2; the coating failed completely with the increased heat flux.

The pre-treatment of a ZrC-SiC feedstock was examined using induction plasma spheroidization (IPS) by Pan et al. (Ref 132). A coating made with this feedstock showed lower consumption during ablation testing compared to coating produced with a spray dried (SD) agglomerated feedstock. The authors suggested that this was due to the reduced porosity in the coating produced with the IPS treated feedstock, allowing a dense, protective oxide scale to form.

Liu et al. (Ref 127) compared the ablation resistance of ZrC-SiC, ZrC-MoS_{i2} and multilayer ZrC-SiC/ZrC-$MoSi_2$ coatings. Both the single-layer coatings were found to offer insufficient protection. While a protective, liquid SiO_2 layer was formed, which filled pores and bonded ZrO_2 on the surface of the ZrC-SiC coating, this caused a layer underneath to become porous as active oxidation of SiC caused SiO to diffuse towards the surface of the coating. The authors believed this would lead to weakened adhesion between the oxidized coating layers and any remaining material beneath, eventually causing failure of the coating. As for the $MoSi_2$ containing coating, the build-up of the oxidation product MoO_3, which unlike other oxidation products CO and CO_2 was unable to pass through the ZrO_2 layer, created a bubble which, when the pressure was high enough, burst and ruptured the coating. In comparison with the single-layer coatings, the multilayer coating performed very well. The outer ZrC-SiC layer was able to form protective SiO_2, which prevented the formation of destructive MoO_3 in the ZrC-$MoSi_2$ inner layer. Oxidation of the inner layer produced Si, which was able to diffuse upwards, oxidize and eliminate the porous lower layer seen in the ZrC-SiC coating. Diagrams for all three of these ablation mechanisms are shown in Fig. 17. In another work looking at ZrC-$MoSi_2$ coatings, by reducing the heat flux from 3.01 to 1.94 MW/m^2, the authors suggested that $MoSi_2$ could be a suitable additive for ablation resistance coatings (Ref 147). The rate of SiO_2 evaporation from the surface was lower than the rate of formation of SiO_2 from the oxidation of $MoSi_2$. A stable SiO_2 layer in turn would prevent the formation of the destructive MoO_3 species, preserving the coating. As $MoSi_2$ content was increased from 0 to 20 to 40 vol. %, the mass ablation rate reduced from −2.80 to −0.92 to −0.68 mg/s, respectively.

While some researchers have had success using SiC containing composites, they are limited by how rapid they can be depleted when active oxidation of SiC occurs and SiO_2 vaporizes and leaves behind a porous structure. Instead of SiC, recent research has focused on the addition

Table 5 A summary of process parameters for thermal spraying of UHTC carbide ceramics

Feedstock	Technique	Particle size (μm)	Spray System	Current (A)	Voltage (V)
ZrC	APS	…	…	120-150	370-410
ZrC	APS	…	…	400-415	125-150
ZrC-LaB_6					
ZrC-SiC					
ZrC/ZrC-SiC	APS	44-74	…	…	…
ZrC-SiC	APS	…	…	400-413	125-135
ZrC-TaC	APS	20-40	…	…	…
ZrC-ZrO_2	APS	…	…	400-415	125-150
ZrC	APS	16.7	Sulzer-Metco F4-MB	…	…
	VPS		Sulzer-Metco F4-VB		
ZrC	VPS	8	Sulzer-Metco F4-VB	500-700	…
ZrC	VPS	…	Sulzer-Metco F4-VB	…	…
ZrC-SiC					
ZrC-TiC					
ZrC-$MoSi_2$	VPS	…	Sulzer-Metco F4-VB	…	…
ZrC-$MoSi_2$	VPS	…	Sulzer-Metco F4-VB	…	…
ZrC-SiC					
ZrC-SiC (IPS)	LPPS	…	Sulzer Metco F4-VB	…	…
ZrC-SiC (SD)					
ZrC-SiC-TiC	VPS	35-40	Sulzer-Metco F4-VB	…	…
ZrC-TiC	VPS	…	Sulzer-Metco F4-VB	…	…
ZrC-SiC					
TiC	APS	…	Sulzer-Metco F4-MB	…	…
TiC	SPS	2.21	Mettech Axial iii	200	…
TiC	CAPS	25	SNMI	593	50
TiC	VPS	10-44	Sulzer-Metco F4-VB	680-720	61-72
TiC	VPS	23.4	Sulzer-Metco F4-VB	…	…
TiC-Mo					
TiC	VPS	17.7	Sulzer-Metco F4-VB	…	…
HfC		8.7			
HfC	VPS	10	Sulzer-Metco F4-VB	800	…
HfC	Suspension VPS	7.08	…	…	…
HfC-TaC	APS	…	…	400-425	120-125
HfC-ZrC-SiC	APS	40-60	…	400	120
TaC	VPS	10-45	Sulzer-Metco EPI	800-1000	40-50
TaC (37,45 & 47 at. % C)	VPS	<50	…	…	…
TaC	VPS	…	Sulzer-Metco F4-MB	…	…
TaC-$MoSi_2$					
TaC-SiC					
TaC-HfC	VPS	<45	…	…	…
TaC-SiC	LPPS	…	Sulzer-Metco F4-VB	…	…

Table 5 continued

Power (kW)	Primary Gas (Ar) Flow (slpm)	Secondary Gas (H_2) Flow (slpm)	Stand-off Distance (mm)	Coating Phases	Microstructural Features	Reference
…	70-80	30-40	100			123
				ZrC, ZrO_2	Dense	
…	75	5-14	100			118, 119
				ZrC, ZrO_2	Dense, un-melted particles on surface	
				ZrC, ZrO_2, LaB_6		
				ZrC, ZrO_2, SiC		
55-65	70-90	20-30	100			121
				ZrC, ZrO_2, SiC	Dense	
…	75	5-15	100			120
				ZrC, ZrO_2, SiC	Dense with SiC particles embedded in ZrC matrix	
33.5	42	5	120			122
				ZrC, TaC, ZrO_2, Ta_2O_5, $TaZr_{2.75}O_8$	Dense microstructure, large, melted splats and small un-melted particles on surface	
…	74	5-15	100			119
				ZrC, ZrO_2	Dense microstructure, un-melted particles on surface	
40	40	10	100			97
				ZrC, ZrO, Zr_2O	ZrC and oxide lamellae with some large pores	
			300			
				ZrC	Lamellar structure with columnar crystals and reduced porosity	
…	50	10	350			128
				ZrC	Dense	
40	40	10	300			129
				…	Fine pores with melted and un-melted particles on surface	
40	40	10	300			147
				ZrC, $MoSi_2$	Some interconnected porosity with melted and un-melted particles on surface	
40	40	10	300			127
				…	Some interconnected porosity with melted and un-melted particles on surface	
41	38	10	300			132
				ZrC, SiC	Fine pores with melted and un-melted particles on surface	
					Some interconnected porosity with melted and un-melted particles on surface	
41	38	10	300			131
				ZrC (peak shifted due to ZrC-TiC solid solution), SiC	Fine pores with melted splats on surface	
40	40	10	300			130
				ZrC (peak shifted due to ZrC-TiC solid solution)	Fine pores and microcracks with melted splats on surface	
				…		
43	29	13	130			68, 115
				TiC, TiO, TiO_2	Lamellar structure with fine pores and microcracks	

Table 5 continued

Power (kW)	Primary Gas (Ar) Flow (slpm)	Secondary Gas (H_2) Flow (slpm)	Stand-off Distance (mm)	Coating Phases	Microstructural Features	Reference
111	…	…	100	TiC, TiO_2, Ti_2O_3, $TiC_{0.1}O_{0.9}$	Lamellar with fine pores	116
…	47	12	100	TiC	Lamellar with fine pores	134
41.5-51.1	35-45	8-12	220	…	Lamellar with some un-melted particles and fine pores	133
41	50	10	260	TiC	Porosity caused my un-melted particles	135
				TiC, Mo	TiC and Mo lamellae with reduced porosity	
50	35	12	220	…	Dense	136, 148
47		10	350			
47.9	30	10	350	HfC	Lamellar structure with fine pores	138
…	20	15	150	HfC, HfO_2, SiC (from bond layer)	Dense with some cracking	139
…	74	5-15	100	HfC, HfO_2, TaC, Ta_2O_5	Fine pores with melted and un-melted particles on surface	125, 126
…	75	5	100	HfC, HfO_2, ZrC, ZrO_2, SiC, SiO_2	Dense microstructure with fully melted and partially melted splats on surface	124
…	…	…	…	TaC, Ta_2C	Lamellar structure in transverse direction, mismatched structure in axial direction with fine porosity	140
…	…	…	…	TaC, Ta_2C, C	Combination of coarse and fine grains	141
…	…	…	…	TaC, Ta_2C	Pores caused by un-melted TaC particles	143
				TaC, Ta_2C, $MoSi_2$		
				TaC, Ta_2C, SiC		
33	…	…	…	Ta(Hf)C, Ta_2C, Ta_4C_3	…	142
…	…	…	…	TaC, Ta_2C	Fine pores with melted and un-melted particles on surface	144

Feedstock	Particle size (μm)	Spray System	Fuel	Oxygen Flow Rate (slpm)	Fuel Flow Rate (slpm)	Power (kW)	Stand-off Distance (mm)	Coating Phases	Microstructural Features	Reference
TiC	2-3	GTV TopGun-G	Ethene	…	…	…	…	TiC, TiO_2	Lamellar with dense oxide and more porous TiC layers	146
TiC-Cr_2O_3	…	…	…	…	…	…	…	…	Melted particles and spherical Cr_2O_3 granules on surface	145

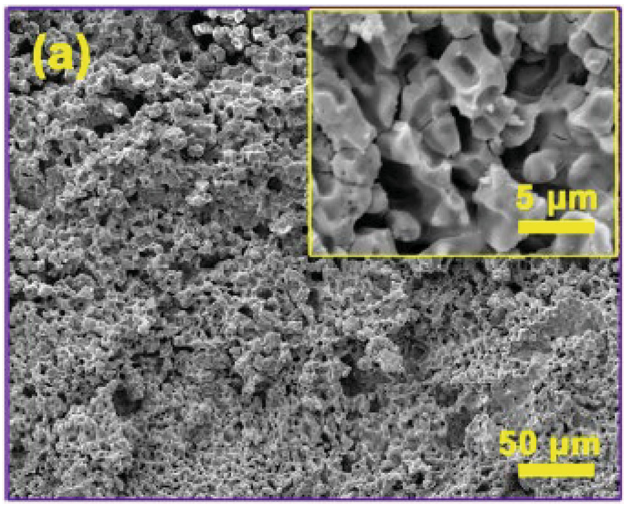

Fig. 15 Porous surface microstructure of ZrC coating after 30 seconds ablation at a heat flux of 2.4 MW/m^2 (Ref 117). Reprinted with permission from Elsevier

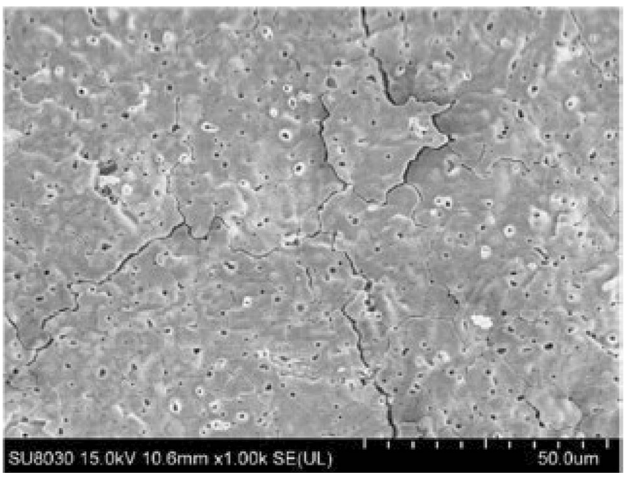

Fig. 16 A relatively dense surface microstructure of a ZrC coating after 30-second ablation test (Ref 128)

of TiC to ZrC-based coatings. While out of all refractory oxides, SiO_2 has the lowest oxygen permeability, meaning a ZrO_2-SiO_2 scale is more protective, TiO_2 has a much lower vaporization rate (0.23 mm/s vs 207 mm/s for SiO_2 at 2500 K), allowing the ZrO_2-TiO_2 scale to offer protection for longer at higher temperatures (Ref 149). Liu et al. (Ref 129) and Pan et al. (Ref 130, 131) have studied the effect of TiC additions to the high temperature properties of ZrC-based coatings. A comparison between ZrC-SiC and ZrC-TiC was made by Liu et al. and Pan et al. (Ref 129, 130). In both cases, the ZrC-TiC coating was found to offer greater protection from ablation due to the increased stability of the protective liquid TiO_2 phase at temperatures higher than 2200 K. Pan et al. also determined an optimized TiC content in the composite coating. At 20 vol. %, a limited amount of TiO_2 was produced, and the oxidized layer was comprised mainly of ZrO_2; thus, rapid oxidation could take place. Increasing the amount of TiC to 30 vol. % promoted the formation of a liquid layer that was not broken during the ablation test, which offered good resistance to ablation. Increasing the TiC level further to 40 vol. % was detrimental to the ablation resistance of the coating. Large amounts of TiO_2 created a composite ZrO_2-TiO_2 liquid with the usually solid ZrO_2 skeleton. The removal of support of the ZrO_2 grains resulted in the removal of the liquid due to the shearing effect of the gas flow, exposing the coating to further oxidation. Further work by Pan et al. (Ref 131) found that increasing the ablation time from 300 to 600 seconds led to a failure of the ZrC-TiC coating due to the increased oxygen permeability of TiO_2.

The addition of LaB_6 to ZrC coatings was studied by Jia et al. (Ref 117, 118). Unlike SiC, which experiences active oxidation above 2000 K, LaB_6 will oxidize to La_2O_3 and then react with ZrO_2 to form $La_2Zr_2O_7$, which has a melting point of 2573 K. After ablation testing at 2592 K the liquid $La_2Zr_2O_7$ protected the ZrO_2 skeleton and stabilized tetragonal ZrO_2 upon cooling to room temperature, reducing the volume change within the oxidized coating.

Jia et al. (Ref 119) experimented with adding 10 and 30 vol. % ZrO_2 to ZrC coating. After coating deposition, XPS found the coatings to contain ZrC, ZrO_2 and ZrC_xO_{1-x} (zirconium oxycarbide), decreasing the C:Zr ratio in the composite coatings. Under ablation conditions, in the 10 vol. % ZrO_2 containing coating, this led to decreased gas evolution, meaning less CO escaped reducing the pores formed in the coating offering less routes for further oxygen diffusion. Increasing the ZrO_2 content in the coating to 30 vol. % had a negative effect; however, excessive ZrO_2 reduced the melting point of the coating and led to increased vaporization.

Along with ZrO_2, HfO_2 has one of the highest melting points among refractory oxides, making HfC another viable coating material for high temperature environments. After ablation testing of a HfC coating at 2273 K, Yoo et al. (Ref 138) reported the formation of a 40 μm glassy HfO_2 layer protecting the remaining HfC coating from oxidation. Despite this, subsequent work from Feng et al. (Ref 125, 126) found that a single-phase HfC coating was not enough to protect from ablation. Similar to the behavior of ZrO_2, the authors reported that when the HfC was oxidized, the HfO_2 became porous and loose, allowing oxygen to diffuse into the coating. In these studies, the authors added 10, 20 and 30 vol. % TaC to HfC coatings. Under ablation, the coatings oxidized to form liquid Ta_2O_5 and solid HfO_2 and $Hf_6Ta_2O_{17}$. At 10 vol. % TaC addition, Ta_2O_5 was able to seal any cracks and pores on the oxide surface, as shown in Fig. 18. As TaC content was increased a composite Ta_2O_5-HfO_2 liquid oxide was formed and subsequently

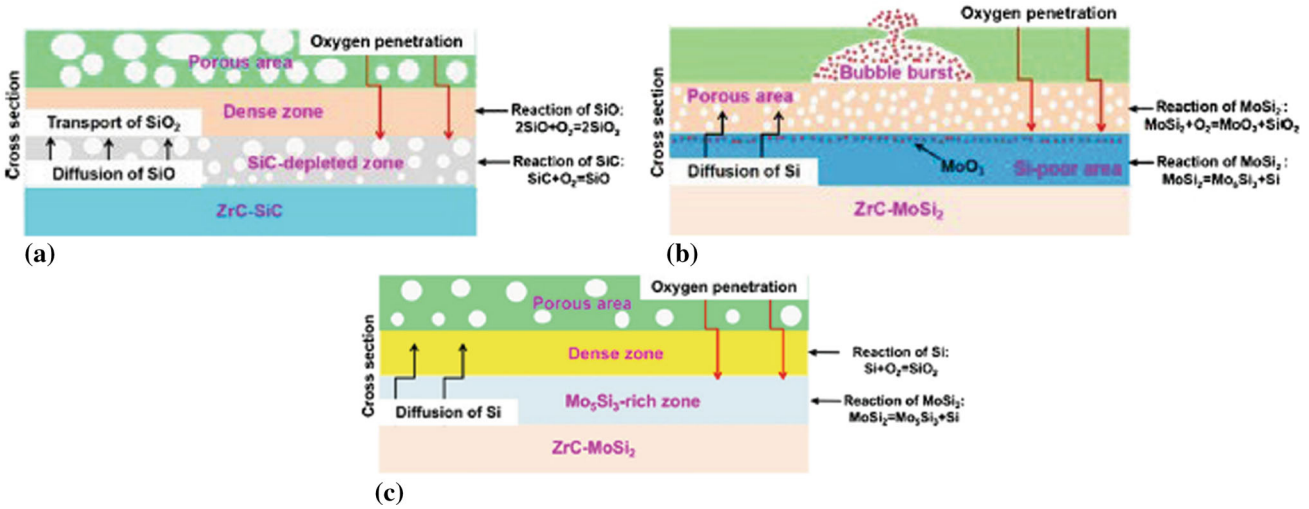

Fig. 17 Schematic diagrams showing the ablation mechanisms of (a) ZrC-SiC coating, (b) ZrC-$MoSi_2$ coating and (c) ZrC-SiC/ZrC-$MoSi_2$ multilayer coating (Ref 127). Reprinted with permission from Elsevier

removed by the shearing effect of the gas flow and exposed the underlying material to further oxidation. A similar effect was noticed by Luo et al. (Ref 122), who tested the ablation resistance of a ZrC-TaC coating and found at high heat fluxes, a Ta_2O_5-ZrO_2 liquid was formed, which was removed mechanically at the ablation centre.

The ablation resistance of TaC coatings themselves has been investigated by Pu et al. (Ref 143) and Niu et al. (Ref 144). Both works found that TaC coatings with SiC additions provided the best protection from ablation. Single-phase TaC coatings oxidized to liquid Ta_2O_5, which was removed by the shearing effect of the gas flow. When SiC was added, a Ta_2O_5-SiO_2 mixed oxide was formed which had a higher density and could withstand erosion.

A summary of the ablation tests conducted on UHTC boride coatings is shown in Table 6. Where possible, the heat flux, surface temperatures and ablation rates have been reported.

Tribology and Wear of UHTC Carbide Coatings

Due to having the highest hardness of the UHTC carbides, TiC is the most widely researched for wear resistant applications. In fact, it is the only thermal spray coating material of all the UHTC carbides to have its tribological properties investigated thoroughly. Hong et al. (Ref 68) prepared a TiC coating using APS, which was subjected to wear test under 20 and 50 N loads against a WC-Co ball. Giving COF of 0.53 and 0.49 and wear rates of 0.07 x 10^{-5} and 2.42 x 10^{-5} mm^3 N^{-1} m^{-1}, respectively, the wear mechanisms were described as fatigue and tribo-oxidation under both sets of conditions. The TiC coating showed much lower wear rates under both loads than a TiB_2 coating tested under the same conditions. In a further study, the authors tested the same TiC coating against a range of different ball materials under 50 N load; specifically, WC-Co, 304 stainless steel and Si_3N_4 balls were used (Ref 115). Against the steel ball, the coating showed a low wear rate of 2.55 x 10^{-6} mm^3 N^{-1} m^{-1} due to the relative softness of the ball. A COF of 0.65 was attributed to the wear debris of the coating acting as an abrasive and ploughing the softer steel ball; some evidence of adhesive wear was also detected. When tested with the Si_3N_4 ball, a low COF of 0.46 and wear rate of 9.76 x 10^{-6} mm^3 N^{-1} m^{-1} were reported, due to the oxidation of the ball to form SiO_2. The fluctuation of COF was high, however, due to the spallation of this oxide. Due to the high hardness of the WC-Co ball, the wear rate was much higher (2.42 x 10^{-5} mm^3 N^{-1} m^{-1}).

The tribological properties of VPS TiC coatings against WC-Co balls were also tested by Guo et al. (Ref 135). After testing under loads of 20 and 50 N, the authors found that the addition of Mo to the coating reduced the wear rate and COF at both conditions. The added ductility of the Mo also helped change the wear mechanism from particle pull-out and fatigue wear to abrasive wear.

An SPS TiC coating was deposited by Mahade et al. (Ref 116); SPS allows the deposition of feedstocks with extremely fine particle sizes, potentially improving wear resistance by reducing splat and pore size. The coating was subjected to a sliding wear test against a WC-Co pin under 5 kgf, which resulted in a 0.2129 mm^3 volume loss and a COF of 0.28.

Srinath et al. (Ref 145) used HVOF thermal spraying to deposit a TiC coating with 10 wt. % Cr_2O_3 addition. The test involved pins and discs being manufactured out of the

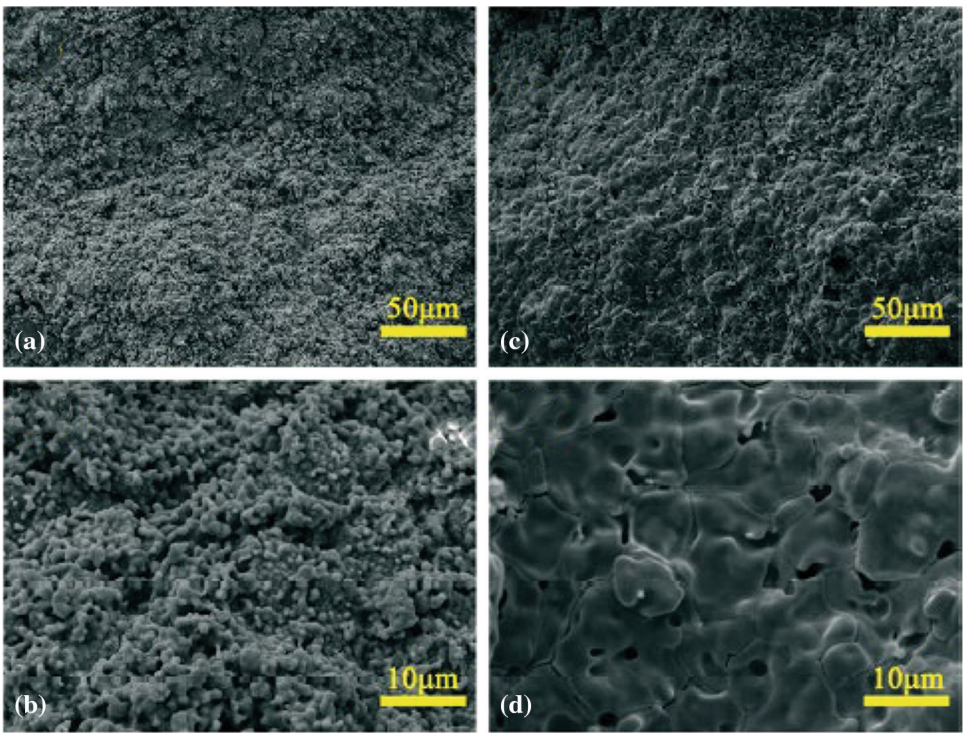

Fig. 18 SEM micrographs showing ZrC + 10 vol. % TaC coating after ablation testing for (a, b) 60 seconds and (c, d) 90 seconds (Ref 125). The increased density of the oxide layer after 90 seconds is clear. Reprinted with permission from Elsevier

coated material and tested at three loads, 0.5, 1 and 2 kg loads. The wear rates, however, were high, which was attributed to poor bonding between the TiC and $C_{r2}O_3$.

Future of UHTC Coatings

Reinforced UHTC Coatings

As explored in previous sections, a range of particle reinforcements (SiC, $MoSi_2$, etc.) to UHTC coatings have already been investigated by researchers, with the primary aim of improving the high temperature performance. As with many ceramics, however, UHTCs suffer from intrinsic brittleness, which can limit their application. Research into sintered UHTCs over the years has covered various toughening mechanisms that can be incorporated into a UHTC composite, largely focussed on continuous fiber reinforcement with C or SiC fibers (Ref 150). While this is not feasible for UHTC coatings, other research has investigated the use of chopped fibers (Ref 151-153), carbon nanotubes (CNTs) (Ref 154-156) and graphene (Ref 157-159) as potential toughening phases. For example, the introduction of 10 vol. % CNTs into a spark plasma sintered HfB_2 ceramic improved the hardness from 18.0 to 21.4 GPa and the fracture toughness from 4.8 to 7.6 MPa $m^{1/2}$ (Ref 154).

Some work on incorporating these into thermal spray ceramic coatings has already been undertaken; CNTs have been incorporated into an APS SiC-based coating by Ariharan et al. (Ref 160), while graphene nanoplatelet (GNP) containing Al_2O_3 and Cr_2O_3 coatings have also been developed (Ref 161-163). Specifically, GNPs were found to improve the fracture toughness and wear resistance of Al_2O_3 and Cr_2O_3 suspension HVOF thermal spray coatings (Ref 161, 162).

High Entropy UHTC Coatings

Borrowing from previous work on high entropy alloys (HEAs) and highentropy ceramics (HECs), high entropy ultra-high temperature ceramics (HE-UHTCs) have garnered significant interest over the last five years (Ref 164, 165). In HE materials, multi-component systems are stabilized to a single phase, and the high configurational entropy has caused improved mechanical properties, wear resistance and high temperature properties (Ref 166). In 2016, Gild et al. (Ref 167) fabricated the first HE-UHTCs. $(Hf_{0.2}Zr_{0.2}Ta_{0.2}Nb_{0.2}Ti_{0.2})B_2$, $(Hf_{0.2}Zr_{0.2}Ta_{0.2}Mo_{0.2}Ti_{0.2})B_2$, $(Hf_{0.2}Zr_{0.2}Mo_{0.2}Nb_{0.2}Ti_{0.2})B_2$, $(Hf_{0.2}Mo_{0.2}Ta_{0.2}Nb_{0.2}Ti_{0.2})B_2$, $(Mo_{0.2}Zr_{0.2}Ta_{0.2}Nb_{0.2}Ti_{0.2})B_2$, and $(Hf_{0.2}Zr_{0.2}Ta_{0.2}Cr_{0.2}Ti_{0.2})B_2$ powders were all synthesized by mixing equimolar amounts of the constituent diboride powders and mechanically alloying via high energy ball milling. While research into HE-UHTCs is still in the early stages, some properties have been characterized. The nanohardness of a $(Hf_{0.2}Nb_{0.2}Ta_{0.2}Zr_{0.2})C$ has been reported as 36.1 GPa, higher than any of the constituent carbides

Table 6 A summary of high temperature tests conducted on UHTC carbide ceramic coatings

Feedstock	Deposition method	Duration (s)	Ablation test type	Heat flux (MW/m^2)	Flame temperature (K)	Surface temperature (K)	Mass ablation rate (mg/s)	Linear ablation rate (um/s)	Reference
ZrC	APS	30	Oxyacetylene flame	…	…	3073	−2	0.9	123
ZrC	VPS	30	Oxyacetylene flame	…	…	2325	−26.7	−3.76	128
ZrC	APS	15	Oxyacetylene flame	4.2	…	…	1.8	…	118
ZrC + 10 vol. % LaB_6							−1.1		
ZrC + 20 vol. % LaB_6							−1		
ZrC + 20 vol. % SiC							1.6		
ZrC	APS	30	Oxyacetylene flame	2.4	…	…	−0.6	−3.2	117
		45				…	0.6	−2	
		90				2498	0.4	1.8	
ZrC + 20 vol. % LaB_6		30				…	−1	−1	
		45				…	−0.9	−0.6	
		90				…	−0.5	−0.2	
		120				2592	−0.3	0.04	
ZrC	VPS	300	Plasma torch	1.9	…	2200	−2.8	…	147
ZrC + 20 vol. % $MoSi_2$						2100	−0.92		
ZrC + 40 vol. % $MoSi_2$						2000	−6.8		
ZrC + 30 vol. % SiC	VPS	300	Plasma torch	3.0	…	2943	−1.42	0.15	127
ZrC + 20 vol. % $MoSi_2$						3003	−0.35	1.3	
ZrC + 20 vol. % $MoSi_2$/ZrC + 30 vol. % SiC						2923	−0.28	0.14	
ZrC	APS	120	Oxyacetylene flame	2.4	…	2498	−0.06	2.25	120
ZrC + 20 vol. % SiC		120				2543	−0.29	0.08	
						2378	0.49	2.5	
						2011	−0.32	−0.67	
		60		4.2		…	2.44	13.87	
ZrC + 30 vol. % SiC (SD)	VPS	60	Plasma torch	…	…	2273	…	…	132
ZrC + 30 vol. % SiC (IPS)									
ZrC/ZrC + 25 vol. % SiC	APS	60	Oxyacetylene flame	…	3273	…	0.8	3.3	121
ZrC	VPS	240	CO_2 laser	15.9	…	2763	…	3.1	129
ZrC + 30 vol. % SiC				15.9		2473		1.9	
				25.5		2601		…	
ZrC + 30 vol. % TiC				15.9		2443		2.3	
				25.5		2673		3.2	
ZrC + 20 vol. % SiC + 10 vol. % TiC	VPS	300	Plasma torch	3.0	…	2636	…	−0.25	131

Table 6 continued

Feedstock	Deposition method	Duration (s)	Ablation test type	Heat flux (MW/m^2)	Flame temperature (K)	Surface temperature (K)	Mass ablation rate (mg/s)	Linear ablation rate (um/s)	Reference
		600						−0.23	
ZrC + 10 vol. % SiC + 20 vol. % TiC		300				2573		−0.7	
		600						−0.22	
ZrC + 30 vol. % TiC		300				2539		−0.67	
		600						…	
ZrC + 30 vol. % SiC		300				2663		−0.22	
		600						−0.13	
ZrC + 20 vol. % TiC	VPS	150	Plasma torch	4.0	…	2539	…	…	130
ZrC + 30 vol. % TiC						2436			
ZrC + 40 vol. % TiC						2398			
ZrC + 20 vol. % SiC						2640			
ZrC + 33 wt. % TaC	APS	20	Oxyacetylene flame	3.2	…	…	7.6	0.5	122
				4.2			12	1.5	
ZrC	APS	30	Oxyacetylene flame	2.4	…	2400	−0.6	−1.4	119
		60					−0.1	−2.4	
		90					0.1	1.4	
ZrC + 10 vol. % ZrO_2		30					−0.2	−0.4	
		60					−0.1	−2.2	
		90					−0.1	1.4	
ZrC + 30 vol. % ZrO_2		30					−0.2	−0.4	
		60					−0.1	−3.6	
		90					−0.1	−2.4	
HfC	VPS	60	Oxyacetylene flame	3.0	…	2273	…	…	138
HfC	Suspension VPS	20	Laser	…	…	2273	0.4 % mass loss	…	139
HfC	APS	40	Oxyacetylene flame	4.2	…	…	0.8	−3.9	126
		60					1.83	…	
HfC + 10 vol. % TaC		40				2431	0.73	−3.71	
		60				…	0.11	−2.16	
HfC	APS	120	Oxyacetylene flame	2.4	…	2201	−0.256	−2.1	125
HfC + 10 vol. % TaC						2280	0.045	−0.302	
HfC + 20 vol. % TaC						2250	−0.251	−1.017	
HfC + 30 vol. % TaC						2180	−0.368	0.742	
HfC/TiC	VPS	30	Plasma wind tunnel	5.9	…	2923	−0.02	…	136

Table 6 continued

Feedstock	Deposition method	Duration (s)	Ablation test type	Heat flux (MW/m^2)	Flame temperature (K)	Surface temperature (K)	Mass ablation rate (mg/s)	Linear ablation rate (um/s)	Reference
HfC + 40 mol. % ZrC + 20 mol. % SiC	APS	30	Oxyacetylene flame	2.4	…	2300	−0.3	…	124
		60					−0.4		
		90					−0.2		
		120					−0.02		
TaC	VPS	60	Plasma torch	…	2473	…	0.99 % mass loss	…	143
TaC + 25 vol. % $MoSi_2$							3.66 % mass loss		
TaC + 25 vol. % SiC							0.99 % mass loss		
TaC + 5 vol. % SiC	LPPS	60	Plasma torch	…	2273	…	0.62 % mass loss	…	144
TaC + 10 vol. % SiC							0.5 % mass loss		
TaC + 15 vol. % SiC							0.15 % mass loss		

(Ref 168). The oxidation behavior of the HE-UHTCs synthesized by Gild et al. (Ref 167) showed that up to 1200 °C weight gain was much lower than some of the constituent borides, for example, TiB_2 and ZrB_2. While HEC and HE-UHTC thermal spray coatings are yet to be developed, HEA coatings have been deposited, using a variety of thermal spray processes, to provide wear, corrosion and oxidation resistance (Ref 169).

Summary

As the next generation of spacecraft and hypersonic flight applications is developed, UHTCs will become materials of great importance because of their high melting points and good mechanical properties. Due to the limitations of current processing methods, only small, simple shaped bulk UHTC components can be formed. To alleviate this problem, UHTC coatings can be employed, and as C- and SiC-based composites become more widely as structural components in aeronautics, protective coatings will be required to protect them from the most extreme of environments. While much work on UHTC coatings has been done outside of the public domain, close collaboration with industrial partners must be sought for future research. Due to the applications UHTC coatings are suited to, this will help produce viable processing conditions that can be achieved on an industrial scale and testing procedures that will represent expected service environments.

This paper has presented a detailed review of UHTC coatings produced by various thermal spray processes. Because of the ultra-high melting temperatures, plasma-based thermal spray techniques have been found to be the most popular for depositing UHTC coatings due to the temperatures which can be reached within the plasma plume itself. To prevent oxidation of UHTC feedstocks, spray systems have often been contained within inert atmospheres or vacuums. While successful at eliminating oxide phases within the coatings, such setups remain expensive. To this end, shrouded plasma spray systems have shown promise as a lower cost alternative; however, further development is needed to deposit completely oxide-free coatings.

The oxidation and ablation resistance of UHTC-based coatings has been widely reported, and the mechanisms are largely understood. Various UHTC composite coatings have been investigated as a means to improve oxidation and ablation resistance, and composite coatings with Si containing materials (such as SiC and $MoSi_2$) have proved to be particularly effective at this. Despite widespread research on the tribology of bulk UHTCs, investigations into the wear resistance of UHTC thermal spray coatings have been sporadic. For example, thin film TiB_2, TiC and

TaC PVD coatings have been investigated to protect tools in the sheet metal forming process from galling, while any application for thermal spray UHTC coatings has yet to be determined (Ref 170, 171). Further research is needed in this domain, especially at elevated temperatures, as the hardness of UHTCs makes them suited to wear resistant applications.

Acknowledgments This work was supported by the Engineering and Physical Sciences Research Council (EPSRC) (grant number EP/M50810X/1).

References

1. R. Loehman et al., Ultrahigh-Temperature Ceramics For Hypersonic Vehicle Applications, *Ind. Heat.*, 2004, **71**(1), p 36-38.
2. J. Justin and A. Jankowiak, Ultra High Temperature Ceramics: Densification Properties and Thermal Stability, *AerospaceLab*, 2011, **3**, p 1-11.
3. R. Savino et al., Arc-Jet Testing on HfB2 and HfC-Based Ultra-High Temperature Ceramic Materials, *J. Eur. Ceram. Soc.*, 2008, **28**(9), p 1899-1907.
4. F. Monteverde and R. Savino, ZrB2-SiC Sharp Leading Edges in High Enthalpy Supersonic Flows, *J. Am. Ceram. Soc.*, 2012, **95**(7), p 2282-2289.
5. S.M. Johnson, et al., Recent developments in ultra high temperature ceramics at NASA Ames. in 16th AIAA/DLR/DGLR International space planes and hypersonic systems and technologies conference (2009)
6. F. Monteverde and R. Savino, Stability of Ultra-High-Temperature ZrB2-SiC Ceramics Under Simulated Atmospheric Re-Entry Conditions, *J. Eur. Ceram. Soc.*, 2007, **27**(16), p 4797-4805.
7. X. Zhang et al., Ablation Behavior of ZrB2-SiC Ultra High Temperature Ceramics Under Simulated Atmospheric Re-Entry Conditions, *Compos. Sci. Technol.*, 2008, **68**(7), p 1718-1726.
8. P.L. Moses et al., NASA Hypersonic Flight Demonstrators—Overview, Status, and Future Plans, *Acta Astronaut.*, 2004, **55**(3), p 619-630.
9. J.K. Sonber et al., Processing of ZrB2- and HfB2-Based Ultra-High Temperature Ceramic Materials: A Review, *Mater. Perform. Charact.*, 2021, **10**(2), p 89-121.
10. B.R. Golla et al., Review on Ultra-High Temperature Boride Ceramics, *Prog. Mater. Sci.*, 2020, **111**, p 100651.
11. M. Kuhn, P. Gold and J. Loos, Wear and friction characteristics of PVD-coated roller bearings, *Surf. Coat. Technol.*, 2004, **177**, p 469-476.
12. Q. Wang et al., Corrosion Behavior of Zirconium Diboride Coated Stainless Steel in Molten 6061 Aluminum Alloy, *Surf. Coat. Technol.*, 2017, **313**, p 129-135.
13. M. Samuelsson et al., ZrB2 Thin Films Grown by High Power Impulse Magnetron Sputtering from a Compound Target, *Thin Solid Films*, 2012, **526**, p 163-167.
14. Y.D. Blum et al., Thick Protective UHTC Coatings for SiC-Based Structures: Process Establishment, *J. Am. Ceram. Soc.*, 2008, **91**(5), p 1453-1460.
15. E.L. Corral and R.E. Loehman, Ultra-High-Temperature Ceramic Coatings for Oxidation Protection of Carbon-Carbon Composites, *J. Am. Ceram. Soc.*, 2008, **91**(5), p 1495-1502.
16. E. Randich and D.D. Allred, Chemically Vapor-Deposited ZrB2 as a Selective Solar Absorber, *Thin Solid Films*, 1981, **83**(4), p 393-398.
17. S. Motojima, K. Funahashi and K. Kurosawa, ZrB2 Coated on Copper Plate by Chemical Vapour Deposition, and its Corrosion and Oxidation Stabilities, *Thin Solid Films*, 1990, **189**(1), p 73-79.
18. E. Lugscheider, et al., Investigations of multifunctional graded zirconium carbide PVD-coatings for the application on machine parts. MRS Online Proceedings Library (OPL) **750** (2002)
19. J. Kohout et al., Hard Multifunctional Hf-B-Si-C Films Prepared by Pulsed Magnetron Sputtering, *Surf. Coat. Technol.*, 2014, **257**, p 301-307.
20. L. Tengdelius et al., Hard and Elastic Epitaxial ZrB2 Thin Films on Al2O3(0001) Substrates Deposited by Magnetron Sputtering from a ZrB2 Compound Target, *Acta Mater.*, 2016, **111**, p 166-172.
21. I. Campbell et al., The Vapor-Phase Deposition of Refractory Materials: I. General Conditions and Apparatus, *J. Electrochem. Soc.*, 1949, **96**(5), p 318.
22. L. Kaufman, E.V. Clougherty, Investigation of boride compounds for very high temperature applications. Manitoba Univ Winnipeg (1963)
23. G. Samsonov et al., Boron and its compounds and alloys [in Russian]. Izd. Akad. Nauk Ukr. SSB, Kiev (1960)
24. G.V. Samsonov and T.I. Serebryakova, Classification of Borides, *Soviet Powder Metall. Metal Ceram.*, 1978, **17**(2), p 116-120.
25. J. He et al., Study of Tribological Properties of Polymer Derived ZrB2-SiC Ceramics, *Ceram. Int.*, 2018, **44**(13), p 15627-15630.
26. W.G. Fahrenholtz et al., Refractory Diborides of Zirconium and Hafnium, *J. Am. Ceram. Soc.*, 2007, **90**(5), p 1347-1364.
27. R.G. Munro, Material Properties of Titanium Diboride, *J. Res. Nat. Inst. Stand. Technol.*, 2000, **105**(5), p 709.
28. H. Okamoto, Supplemental Literature Review of Binary Phase Diagrams: Ag-Ca, Al-Yb, As-Fe, B-Zr, Co-U, Cu-Se, Cu-Th, La-Mo, Mg-Sn, Mo-Th, Sn-Ta, and Te-Ti, *J. Phase Equilib. Diffus.*, 2017, **38**(6), p 929-941.
29. H. Okamoto, T. Massalski, Binary alloy phase diagrams. ASM International, Materials Park, OH, USA (1990)
30. H. Okamoto, Supplemental Literature Review of Binary Phase Diagrams: Al-Ni, B-Hf, Ca-Sc, Cr-Sc, Fe-Rh, Hf-Mn, La-Sb, Ni-Re, Ni-Sm, Ni-Zr, Sb-Tb, and Ti-Zr, *J. Phase Equilib. Diffus.*, 2019, **40**(6), p 830-841.
31. V.A. Lavrenko et al., The Oxidation of ZrB2, TaB2, NbB2, and W2B5 in Atomic Oxygen and by Anodic Polarization, *Oxid. Met.*, 1974, **8**(3), p 131-137.
32. W.C. Tripp and H.C. Graham, Thermogravimetric Study of the Oxidation of ZrB2 in the Temperature Range of 800° to 1500°C, *J. Electrochem. Soc.*, 1971, **118**(7), p 1195.
33. W.G. Fahrenholtz and G.E. Hilmas, Oxidation of Ultra-High Temperature Transition Metal Diboride Ceramics, *Int. Mater. Rev.*, 2012, **57**(1), p 61-72.

34. Y.H. Koh, S.Y. Lee and H.E. Kim, Oxidation Behavior of Titanium Boride at Elevated Temperatures, *J. Am. Ceram. Soc.*, 2001, **84**(1), p 239-241.
35. T. Parthasarathy et al., A Model for the Oxidation of ZrB2, HfB2 and TiB2, *Acta Mater.*, 2007, **55**(17), p 5999-6010.
36. H. Probst and W. Sanders, High temperature mechanical properties of polycrystalline hafnium carbide and hafnium carbide containing 13-volume-percent hafnium diboride (1969)
37. E. Wuchina and M. Opeka, The Group IV carbides and nitrides, p. 361-390 (2014)
38. M.C.L. Patterson et al., Advanced HfC-TaC Oxidation Resistant Composite Rocket Thruster, *Mater. Manuf. Processes*, 1996, **11**(3), p 367-379.
39. R.W. Newman, Oxidation-Resistant High-Temperature Materials, *J. Hopkins APL Tech. Dig.*, 1993, **14**(1), p 24-28.
40. Y. Katoh et al., Properties of Zirconium Carbide for Nuclear Fuel Applications, *J. Nucl. Mater.*, 2013, **441**(1), p 718-742.
41. A. Miyoshi and A. Hara, High Temperature Hardness of WC, TiC, TaC, NbC and Their Mixed Carbides, *J. Jpn. Soc. Powder Powder Metall.*, 1965, **12**(2), p 78-84.
42. W.D. Sproul, Reactively Sputtered Nitrides and Carbides of Titanium, Zirconium, and Hafnium, *J. Vac. Sci. Technol., A: Vac., Surf. Films*, 1986, **4**(6), p 2874-2878.
43. G.R. Fenske, Nitride and Carbide Coatings for High Speed Steel Cutting Tools, *Tribol. Trans.*, 1989, **32**(3), p 339-345.
44. E. Wuchina et al., Designing for Ultrahigh-Temperature Applications: The Mechanical and Thermal Properties of HfB2, HfCx, HfNxand Hf(N), *J. Mater. Sci.*, 2004, **39**(19), p 5939-5949.
45. M.M. Opeka et al., Mechanical, Thermal, and Oxidation Properties of Refractory Hafnium and Zirconium Compounds, *J. Eur. Ceram. Soc.*, 1999, **19**(13-14), p 2405-2414.
46. R.W. Harrison and W.E. Lee, Processing and Properties of ZrC, ZrN and ZrCN Ceramics: A Review, *Adv. Appl. Ceram.*, 2016, **115**(5), p 294-307.
47. M. Bauccio, *ASM Engineered Materials Reference Book,* ASM International, USA, 1994.
48. X. Zhang, G.E. Hilmas and W.G. Fahrenholtz, Densification and Mechanical Properties of TaC-Based Ceramics, *Mater. Sci. Eng., A*, 2009, **501**(1), p 37-43.
49. J.-X. Liu, X. Huang and G.-J. Zhang, Pressureless Sintering of Hafnium Carbide-Silicon Carbide Ceramics, *J. Am. Ceram. Soc.*, 2013, **96**(6), p 1751-1756.
50. A. Teber et al., Effect of SPS Process Sintering on the Microstructure and Mechanical Properties of Nanocrystalline TiC for Tools Application, *Int. J. Refract Metal Hard Mater.*, 2012, **30**(1), p 64-70.
51. J.F. Shackelford and W. Alexander, *CRC Materials Science and Engineering Handbook*, CRC Press, USA, 2000.
52. H. O. Pierson, *Handbook of Refractory Carbides and Nitrides: Properties, Characteristics, Processing and Applications,* Noyes Publication, USA, 1996.
53. S. Kovacevic et al., Interfacial Energy as the Driving Force for Diffusion Bonding of Ceramics, *Acta Mater.*, 2020, **186**, p 405-414.
54. H. Okamoto, Supplemental Literature Review of Binary Phase Diagrams: Au-Dy, Au-Sc, Au-Yb, C-Hf, C-Ta, Cu-Fe, Dy-Mn, Er-Mn, Ho-Mn, Mn-Tb, Mn-Tm, and Sb-Sn, *J. Phase Equilib. Diffus.*, 2017, **38**(2), p 160-170.
55. S. Shimada and K. Mochidsuki, The Oxidation of TiC in Dry Oxygen, Wet Oxygen, and Water Vapor, *J. Mater. Sci.*, 2004, **39**(2), p 581-586.
56. M. Desmaison-Brut, N. Alexandre and J. Desmaison, Comparison of the Oxidation Behaviour of Two Dense Hot Isostatically Pressed Tantalum Carbide (TaC and Ta2C) Materials, *J. Eur. Ceram. Soc.*, 1997, **17**(11), p 1325-1334.
57. S. Shimada, A Thermoanalytical Study on the Oxidation of ZrC and HfC Powders with Formation of Carbon, *Solid State Ionics*, 2002, **149**(3), p 319-326.
58. V.A. Lavrenko et al., High-Temperature Oxidation of Titanium Carbide in Oxygen, *Oxid. Met.*, 1975, **9**(2), p 171-179.
59. M.M. Opeka, I.G. Talmy and J.A. Zaykoski, Oxidation-Based Materials Selection for 2000°C + Hypersonic Aerosurfaces: Theoretical Considerations and Historical Experience, *J. Mater. Sci.*, 2004, **39**(19), p 5887-5904.
60. E. Wuchina et al., UHTCs: Ultra-High Temperature Ceramic Materials for Extreme Environment Applications, *Electrochem. Soc. Interface*, 2007, **16**(4), p 30-36.
61. G.A. Rama Rao and V. Venugopal, Kinetics and Mechanism of the Oxidation of ZrC, *J. Alloys Compd..*, 1994, **206**(2), p 237-242.
62. C. Bargeron et al., Oxidation of Hafnium Carbide in the Temperature Range 1400-2060°C, *J. Am. Ceram. Soc.*, 2005, **76**, p 1040-1046.
63. D. Tejero-Martin et al., Beyond Traditional Coatings: A Review on Thermal-Sprayed Functional and Smart Coatings, *J. Therm. Spray Technol.*, 2019, **28**(4), p 598-644.
64. M.F. Morks, I. Cole and A. Kobayashi, Plasma Forming Multilayer Ceramics for Ultra-High Temperature Application, *Vacuum*, 2013, **88**, p 134-138.
65. J. Xu et al., Fabrication and Properties of ZrC-ZrB2/Ni Cermet Coatings on a Magnesium Alloy by Atmospheric Plasma Spraying of SHS Powders, *Ceram. Int.*, 2014, **40**, p 15537-15544.
66. X. Feng et al., Oxidation Behaviour of Plasma-Sprayed ZrB2-SiC Coatings, *Ceram. Int.*, 2019, **45**(2), p 2385-2392.
67. O.N. Grigoriev et al., Structural and Phase Transformations in Plasma-Spray ZrB2-SiC-AlN Coatings on a C/C-SiC Substrate After High-Temperature Thermal Cyclic Heating, *Powder Metall. Met. Ceram.*, 2019, **58**(5-6), p 341-350.
68. D. Hong et al., Comparison of Microstructure and Tribological Properties of Plasma-Sprayed TiN, TiC and TiB2 Coatings, *Surf. Coat. Technol.*, 2019, **374**, p 181-188.
69. S. Sun et al., Ablation Mechanism and Properties of SiO2 Modified ZrB2-SiC Coatings Fabricated on C/C Composites via Plasma Spraying Technology, *Surf. Coat. Technol.*, 2020, **381**, p 125132.
70. X. Yao et al., Ablation Behavior of ZrB2-Based Coating Prepared by Supersonic Plasma Spraying for SiC-Coated C/C Composites Under Oxyacetylene Torch, *J. Therm. Spray Technol.*, 2013, **22**(4), p 531-537.
71. Y. Zhang et al., Ablation Resistance of ZrB2-SiC Coating Prepared by Supersonic Atmosphere Plasma Spraying for SiC-Coated Carbon/Carbon Composites, *Ceram. Int.*, 2014, **40**, p 14749-14755.
72. K. Li, G. Liu and Y. Zhang, Ablation properties of HfB2 coatings prepared by supersonic atmospheric plasma spraying for SiC-coated carbon/carbon composites, *Surf. Coat. Technol.*, 2019, **357**, p 48-56.
73. J. Hu et al., Influence of High-Enthalpy Atmospheric Plasma Spraying Power on Oxidation Resistance of ZrB2-LaF3 Coatings, *Surf. Coat. Technol.*, 2021, **410**, p 126975.
74. A. Killinger et al., Review of New Developments in Suspension and Solution Precursor Thermal Spray Processes, *J. Therm. Spray Technol.*, 2011, **20**(4), p 677-695.
75. E. Yvenou, et al., TiB2 Deposited on Graphite by Suspension Plasma Spray as Al Wettable Cathode, *J. Therm. Spray Technol.*, 2021, **30**, p 1535-1543.
76. B. Ma and J. Li, ZrB2-SiC-ZrC Coating on ZrC Ceramics Deposited by Plasma Spraying, *Results Phys.*, 2019, **15**, p 102550.

77. B.A. Kahl, C.C. Berndt and A.S.M. Ang, Boride-based Ultra-High Temperature Ceramic Coatings Deposited via Controlled Atmosphere Plasma Spray, *Surf. Coat. Technol.*, 2021, **416**, p 127128.
78. Y. Niu et al., Comparison of ZrB2-MoSi2 Composite Coatings Fabricated by Atmospheric and Vacuum Plasma Spray Processes, *J. Therm. Spray Technol.*, 2017, **26**(1-2), p 100-107.
79. J.H. Liu, B. Blanpain and P. Wollants, A XPS Study of Atmospheric Plasma Sprayed TiB2 Coatings, *Key Eng. Mater.*, 2008, **368-372**, p 1347-1350.
80. P. Fauchais Thermal spray fundamentals: from powder to part, ed. J.V. Heberlein and M.I. Boulos. (Springer,London, 2014)
81. M. Tului et al., Some Properties of Atmospheric Air and Inert Gas High-Pressure Plasma Sprayed ZrB2 Coatings, *Surf. Coat. Technol.*, 2002, **151-152**, p 483-489.
82. M. Tului, G. Marino and T. Valente, Plasma Spray Deposition of Ultra High Temperature Ceramics, *Surf. Coat. Technol.*, 2006, **201**(5), p 2103-2108.
83. G. Pulci et al., High Temperature Mechanical Behavior of UHTC Coatings for Thermal Protection of Re-Entry Vehicles, *J. Therm. Spray Technol.*, 2011, **20**(1-2), p 139-144.
84. M. Tului et al., Silicon Carbide Based Plasma Sprayed Coatings, *Surf. Coat. Technol.*, 2012, **207**, p 182-189.
85. Y. Niu et al., Oxidation and Ablation Resistance of Low Pressure Plasma-Sprayed ZrB2-Si Composite Coating, *J. Therm. Spray Technol.*, 2014, **23**(3), p 470-476.
86. R.-Q. Wang et al., Low-Pressure Plasma Spraying of ZrB2-SiC Coatings on C/C Substrate by Adding TaSi2, *Surf. Coat. Technol.*, 2021, **420**, p 127332.
87. C. Bartuli, T. Valente and M. Tului, Plasma Spray Deposition and High Temperature Characterization of ZrB2-SiC Protective Coatings, *Surf. Coat. Technol.*, 2002, **155**(2-3), p 260-273.
88. W. Tan, C.A. Petorak and R.W. Trice, Rare-Earth Modified Zirconium Diboride High Emissivity Coatings for Hypersonic Applications, *J. Eur. Ceram. Soc.*, 2014, **34**(1), p 1-11.
89. R. Aliasgarian et al., The Ablation Behavior of ZrB2-SiC Coating Prepared by Shrouded Plasma Spray on SiC-Coated Graphite, *J. Alloy. Compd.*, 2018, **742**, p 797-803.
90. S. Torabi, Z. Valefi and N. Ehsani, Ablation Behavior of SiC/ZrB2 Multilayer Coating Prepared by Plasma Spray Method, *Metall. Mater. Trans. A.*, 2020, **51**(3), p 1304-1319.
91. P. Karuna Purnapu Rupa et al., Microstructure and Phase Composition of Composite Coatings Formed by Plasma Spraying of ZrO2 and B4C Powders, *J. Therm. Spray Technol.*, 2010, **19**(4), p 816-823.
92. G.-J. Zhang et al., Ultrahigh Temperature Ceramics (UHTCs) Based on ZrB2and Hfb2systems: Powder Synthesis, Densification and Mechanical Properties, *J. Phys. Conf. Series*, 2009, **176**, p 012041.
93. Z. Mao et al., Comparison of the Coatings Deposited Using Ti and B4C Powder by Reactive Plasma Spraying in Air and Low Pressure, *J. Mater. Sci.*, 2009, **44**(12), p 3265-3272.
94. J.J. Moore and H.J. Feng, Combustion Synthesis of Advanced Materials: Part I Reaction Parameters, *Progress Mater. Sci.*, 1995, **39**(4-5), p 243-273.
95. S. Cheng et al., Laser Ablation Behavior and Mechanism of C/SiC Coated with ZrB2 -MoSi2-SiC/Mo Prepared by HVOF, *Ceram. Int.*, 2020, **46**(11), p 17752-17762.
96. K. Korpiola, et al. Oxygen partial pressure measurement in the HVOF gun tail flame. in Proceedings of the 8th National Thermal Spray Conference (1995)
97. C. Hu et al., Influence of Oxidation Behavior of Feedstock on Microstructure and Ablation Resistance of Plasma-Sprayed Zirconium Carbide Coating, *J. Therm. Spray Technol.*, 2015, **24**(7), p 1302-1311.
98. E.M. Alosime, M.S. Alsuhybani and M.S. Almeataq, The Oxidation Behavior of ZrB2-SiC Ceramic Composites Fabricated by Plasma Spray Process, *Materials*, 2021, **14**(2), p 392.
99. X. Jin et al., Advances in Oxidation and Ablation Resistance of High and Ultra-High Temperature Ceramics Modified or Coated Carbon/Carbon Composites, *J. Eur. Ceram. Soc.*, 2018, **38**(1), p 1-28.
100. J. Han et al., Oxidation-Resistant ZrB2-SiC Composites at 2200°C, *Compos. Sci. Technol.*, 2008, **68**(3), p 799-806.
101. T.S.R.C. Murthy et al., Tribological Properties of TiB2 and TiB2-MoSi2 Ceramic Composites, *J. Eur. Ceram. Soc.*, 2006, **26**(7), p 1293-1300.
102. J.K. Sonber et al., Friction and Wear Properties of Zirconium Diboride in Sliding Against WC Ball, *Int. J. Refract Metal Hard Mater.*, 2018, **76**, p 41-48.
103. S. Chakraborty et al., Densification, Mechanical and Tribological Properties of ZrB2 by SPS: Effect of Pulsed Current, *Int. J. Refract Metal Hard Mater.*, 2015, **48**, p 150-156.
104. V. Verma, V. Cheverikin and R. Câmara Cozza, Review: Effect on Physical, Mechanical, and Wear Performance of ZrB 2 -Based Composites Processed with or Without Additives, *Int. J. Appl. Ceramic Technol.*, 2020, **17**(6), p 2509-2532.
105. D. Medved' et al., Wear Resistance of ZrB2 Based Ceramic Composites, *Int. J. Refract Metal Hard Mater.*, 2019, **81**, p 214-224.
106. R. Wäsche, D. Klaffke and T. Troczynski, Tribological Performance of SiC and TiB2 Against SiC and Al2O3 at Low Sliding Speeds, *Wear*, 2004, **256**(7-8), p 695-704.
107. S. Dallaire and R.G. Saint-Jacques, Plasma-Sprayed TiC Protective Coatings for Fusion Devices: Coating Fabrication Criteria, *Surf. Coat. Technol.*, 1987, **33**, p 319-326.
108. F. Brossa, G. Rigon and B. Looman, Behaviour of Plasma Spray Coatings Under Disruption Simulation, *J. Nucl. Mater.*, 1988, **155-157**, p 267-272.
109. F. Bordeaux, R.G. Saint Jacques and C. Moreau, Study of Surface Preparation for Enhanced Resistance to Thermal Shocks of Plasma-Sprayed TiC Coatings, *Surf. Coat. Technol.*, 1991, **49**(1), p 50-56.
110. H.D. Steffens, M. Dvorak and P. Groot, Thermal Behaviour of Thick TiC Layers Made by Plasma Spraying, *Surf. Coat. Technol.*, 1991, **49**(1-3), p 46-49.
111. R.G. Saint-Jacques et al., Enhanced Resistance of Plasma-Sprayed TiC Coatings to Thermal Shocks, *J. Nucl. Mater.*, 1992, **191-194**, p 465-468.
112. J. Matějíček, P. Chráska and J. Linke, Thermal Spray Coatings for Fusion Applications—Review, *J. Therm. Spray Technol.*, 2007, **16**(1), p 64-83.
113. D. Fournier et al., Transmission Electron Microscopy Characterization of Plasma Sprayed TiC Coatings, *J. Vac. Sci. Technol., A: Vac., Surf. Films*, 1985, **3**(6), p 2475-2478.
114. P. Groot et al., Plasma-Sprayed Titanium Carbide Coatings for First-Wall Applications in Fusion Devices, *J. Nucl. Mater.*, 1991, **179-181**, p 370-374.
115. D. Hong et al., Comparative Study on Wear Behavior of Plasma-Sprayed TiC Coating Sliding Against Different Counterparts, *J. Therm. Spray Technol.*, 2020, **29**(5), p 1082-1092.
116. S. Mahade et al., Exploiting Suspension Plasma Spraying to Deposit Wear-Resistant Carbide Coatings, *Materials*, 2019, **12**(15), p 2344.
117. Y. Jia et al., Ablation Behavior of Rare Earth La-Modified ZrC Coating for SiC-Coated Carbon/Carbon Composites Under an Oxyacetylene Torch, *Corros. Sci.*, 2016, **104**, p 61-70.
118. Y. Jia et al., Effect of Monolithic LaB6 on the Ablation Resistance of ZrC/SiC Coating Prepared by Supersonic Plasma Spraying for C/C Composites, *J. Mater. Sci. Technol.*, 2016, **32**(10), p 996-1002.

119. Y. Jia et al., Ablation Resistance of Supersonic-Atmosphere-Plasma-Spraying ZrC Coating Doped with ZrO2 for SiC-Coated Carbon/Carbon Composites, *Corros. Sci.*, 2017, **123**, p 40-54.
120. Y. Jia et al., Ablation Resistance of SiC-Modified ZrC Coating Prepared by SAPS for SiC-Coated Carbon/Carbon Composites, *Int. J. Appl. Ceram. Technol.*, 2017, **14**(3), p 331-343.
121. D.-J. Yao et al., Ablation Resistance of ZrC/SiC Gradient Coating for SiC-Coated Carbon/Carbon Composites Prepared by Supersonic Plasma Spraying, *J. Eur. Ceram. Soc.*, 2016, **36**(15), p 3739-3746.
122. X. Luo et al., Ablative Property and Mechanism of ZrC-TaC/ZrC-SiC Coatings on C/C Composites under Different Heat Fluxes, *J. Therm. Spray Technol*., 2021, **30**, p 1582-1594.
123. H. Wu et al., Microstructures and Ablation Resistance of ZrC Coating for SiC-Coated Carbon/Carbon Composites Prepared by Supersonic Plasma Spraying, *J. Therm. Spray Technol.*, 2011, **20**(6), p 1286-1291.
124. Y. Yang et al., HfC-ZrC-SiC Multiphase Protective Coating for SiC-Coated C/C Composites Prepared by Supersonic Atmospheric Plasma Spraying, *Ceram. Int.*, 2017, **43**(1), p 1495-1503.
125. G. Feng et al., Investigation on the Ablation Performance and Mechanism of HfC Coating Modified with TaC, *Corros. Sci.*, 2020, **170**, p 108649.
126. G. Feng et al., Effect of Tantalum Carbide on the Ablation Behaviors of Hafnium Carbide Coating for C/C Composites Under Single and Cyclic Oxyacetylene Torch Environments, *Surface Coat. Technol.*, 2020, **400**, p 126219.
127. T. Liu et al., Ablation Resistance of ZrC-MoSi2/ZrC-SiC Double-Layered Coating in a Plasma Flame, *Corros. Sci.*, 2018, **145**, p 239-248.
128. B. Kang et al., Characteristics of ZrC Barrier Coating on SiC-Coated Carbon/Carbon Composite Developed by Thermal Spray Process, *Materials*, 2019, **12**(5), p 747.
129. T. Liu et al., Laser Ablation Behaviors of Vacuum Plasma Sprayed ZrC-Based Coatings, *J. Am. Ceram. Soc.*, 2019, **102**(7), p 4247-4258.
130. X. Pan et al., Ablation Behaviors of ZrC-TiC Coatings Prepared by Vacuum Plasma Spray: Above 2000 °C, *J. Eur. Ceram. Soc.*, 2019, **39**(11), p 3292-3300.
131. X. Pan et al., Long Time Ablation Behaviors of Designed ZrC-SiC-TiC Ternary Coatings for Environments Above 2000 °C, *Corros. Sci.*, 2020, **170**, p 108645.
132. X. Pan et al., Relationship Analysis on Particle-Coating-Ablation Property of UHTC Coatings Fabricated by Plasma Spray Technique, *Ceram. Int.*, 2021, **47**(3), p 3808-3815.
133. D.J. Varacalle et al., Titanium Carbide Coatings Fabricated by the Vacuum Plasma Spraying Process, *Surf. Coat. Technol.*, 1996, **86-87**, p 70-74.
134. M. Leylavergne et al., Comparison of Plasma-Sprayed Coatings Produced in Argon or Nitrogen Atmosphere, *J. Therm. Spray Technol.*, 1998, **7**(4), p 527-536.
135. X. Guo et al., Microstructure and Tribological Property of TiC-Mo Composite Coating Prepared by Vacuum Plasma Spraying, *J. Therm. Spray Technol.*, 2012, **21**(5), p 1083-1090.
136. H.S. Kim, B.R. Kang and S.M. Choi, Fabrication and Characteristics of a HfC/TiC Multilayer Coating by a Vacuum Plasma Spray Process to Protect C/C Composites Against Oxidation, *Corros. Sci.*, 2021, **178**, p 109068.
137. M. Boncoeur, G. Schnedecker, and J. Lulewicz. HfC plasma coating of C/C composites. in 16th Annual Conference on Composites and Advanced Ceramic Materials. 1992
138. H.-I. Yoo et al., Hafnium Carbide Protective Layer Coatings on Carbon/Carbon Composites Deposited with a Vacuum Plasma Spray Coating Method, *J. Eur. Ceram. Soc.*, 2016, **36**(7), p 1581-1587.
139. Y.W. Yoo et al., Hafnium Carbide Coatings Deposited by Suspension Vacuum Plasma Spraying for Ultra-High-Temperature Oxidation Barrier on Carbon Composites, *Appl. Sci. Converg. Technol.*, 2021, **30**(1), p 21-24.
140. K. Balani et al., Synthesis, Microstructural Characterization, and Mechanical Property Evaluation of Vacuum Plasma Sprayed Tantalum Carbide, *J. Am. Ceram. Soc.*, 2006, **89**(4), p 1419-1425.
141. R.A. Morris et al., Variations in Tantalum Carbide Microstructures with Changing Carbon Content, *Int. J. Appl. Ceram. Technol.*, 2013, **10**(3), p 540-551.
142. B.C. Schulz et al., Influence of Hafnium Carbide on Vacuum Plasma Spray Processed Tantalum Carbide Microstructures, *J. Eur. Ceram. Soc.*, 2013, **33**(6), p 1219-1224.
143. H. Pu et al., Ablation of Vacuum Plasma Sprayed TaC-Based Composite Coatings, *Ceram. Int.*, 2015, **41**(9), p 11387-11395.
144. Y. Niu et al., Microstructure and Ablation Property of TaC-SiC Composite Coatings, *Key Eng. Mater.*, 2016, **697**, p 535-538.
145. M.K. Srinath et al., Micro-Structural, Physical and Tribological Properties of HVOF Spayed (TiC + Cr2O3) Composite Coatings, *Materials Today: Proceedings*, 2021, **44**, p 554-560.
146. A. Förg et al., Suspension and Coating Characterization of High Velocity Suspension Flame Sprayed (HVSFS) Mixed Titanium Oxide-Titanium Carbide Coatings, *Surf. Coat. Technol.*, 2019, **371**, p 90-96.
147. T. Liu et al., Effect of MoSi2 Addition on Ablation Behavior of ZrC Coating Fabricated by Vacuum Plasma Spray, *Ceram. Int.*, 2018, **44**(8), p 8946-8954.
148. H.S. Kim, B.R. Kang and S.M. Choi, Microstructure and Mechanical Properties of Vacuum Plasma Sprayed HfC, TiC, and HfC/TiC Ultra-High-Temperature Ceramic Coatings, *Materials*, 2019, **13**(1), p 124.
149. A. Bronson and J. Chessa, An Evaluation of Vaporizing Rates of SiO2 and TiO2 as Protective Coatings for Ultrahigh Temperature Ceramic Composites, *J. Am. Ceram. Soc.*, 2008, **91**(5), p 1448-1452.
150. J. Binner et al., Selection, Processing, Properties and Applications of Ultra-High Temperature Ceramic Matrix Composites, UHTCMCs - a Review, *Int. Mater. Rev.*, 2020, **65**(7), p 389-444.
151. L. Silvestroni et al., Relationships Between Carbon Fiber Type and Interfacial Domain in ZrB2-Based Ceramics, *J. Eur. Ceram. Soc.*, 2016, **36**(1), p 17-24.
152. J. Sha et al., ZrB2-Based Composites Toughened by as-Received and Heat-treated Short Carbon Fibers, *J. Eur. Ceram. Soc.*, 2017, **37**(2), p 549-558.
153. D. Sciti and L. Silvestroni, Processing, Sintering and Oxidation Behavior of SiC Fibers Reinforced ZrB2 Composites, *J. Eur. Ceram. Soc.*, 2012, **32**(9), p 1933-1940.
154. H. Jin et al., HfB2-CNTs Composites with Enhanced Mechanical Properties Prepared by Spark Plasma Sintering, *Ceram. Int.*, 2017, **43**(2), p 2170-2173.
155. J. Lin et al., Microstructure and Mechanical Properties of Spark Plasma Sintered ZrB2-SiC-MWCNT Composites, *Ceramics Int.*, 2015, **41**, p 15261-15265.
156. R.B. Acicbe and G. Goller, Densification Behavior and Mechanical Properties of Spark Plasma-Sintered ZrC-TiC and ZrC-TiC-CNT Composites, *J. Mater. Sci.*, 2013, **48**(6), p 2388-2393.
157. G.B. Yadhukulakrishnan et al., Spark Plasma Sintering of Graphene Reinforced Zirconium Diboride Ultra-High Temperature Ceramic Composites, *Ceram. Int.*, 2013, **39**(6), p 6637-6646.
158. Y. Cheng et al., Using Macroporous Graphene Networks to Toughen ZrC-SiC Ceramic, *J. Eur. Ceram. Soc.*, 2018, **38**(11), p 3752-3758.

159. M.A. Shahedi, B. Nayebi and M. Shokouhimehr, TEM Characterization of Spark Plasma Sintered ZrB2-SiC-Graphene Nanocomposite, *Ceramics Int.*, 2018, **44**(13), p 15269-15273.
160. S. Ariharan et al., Dual-Layer Oxidation-Protective Plasma-Sprayed SiC-ZrB2/Al2O3-Carbon Nanotube Coating on Graphite, *J. Therm. Spray Technol.*, 2017, **26**(3), p 417-431.
161. J.W. Murray et al., Alumina-Graphene Nanocomposite Coatings Fabricated by Suspension High Velocity Oxy-Fuel Thermal Spraying for Ultra-Low-Wear, *J. Eur. Ceram. Soc.*, 2018, **38**(4), p 1819-1828.
162. F. Venturi, J. Pulsford and T. Hussain, A Novel Approach to Incorporate Graphene Nanoplatelets to Cr2O3 for Low-Wear Coatings, *Mater. Lett.*, 2020, **276**, p 128283.
163. X. Wu et al., Enhancing Graphene Retention and Electrical Conductivity of Plasma-Sprayed Alumina/Graphene Nanoplatelets Coating by Powder Heat Treatment, *Coatings*, 2021, **11**(6), p 643.
164. A. Nisar et al., A Perspective on Challenges and Opportunities in Developing High Entropy-Ultra High Temperature Ceramics, *Ceramics Int.*, 2020, **46**, p 25845-25853.
165. L. Feng, W.G. Fahrenholtz and D.W. Brenner, High-Entropy Ultra-High-Temperature Borides and Carbides: A New Class of Materials for Extreme Environments, *Annu. Rev. Mater. Res.*, 2021, **51**(1), p 165-185.
166. Y. Zhang et al., Microstructures and Properties of High-Entropy Alloys, *Prog. Mater Sci.*, 2014, **61**, p 1-93.
167. J. Gild et al., High-Entropy Metal Diborides: A New Class of High-Entropy Materials and a New Type of Ultrahigh Temperature Ceramics, *Sci. Rep.*, 2016, **6**(1), p 37946.
168. E. Castle et al., Processing and Properties of High-Entropy Ultra-High Temperature Carbides, *Sci. Rep.*, 2018, **8**(1), p 8609.
169. A. Meghwal et al., Thermal Spray High-Entropy Alloy Coatings: a Review, *J. Therm. Spray Technol.*, 2020, **29**, p 857-893.
170. O. Wänstrand, R. Fella and N. Axén, A Tribological Study of PVD Coatings with Carbon-Rich Outer Layers, *Surf. Coat. Technol.*, 1997, **94-95**, p 469-475.
171. B. Podgornik, S. Hogmark and O. Sandberg, Proper Coating Selection for Improved Galling Performance of Forming Tool Steel, *Wear*, 2006, **261**(1), p 15-21.